RSC Advances

PAPER

View Article Online
View Journal | View Issue

Cite this: *RSC Adv.*, 2025, **15**, 15670

Structural, optical, and electrochemical properties of tungsten-doped cadmium zinc phosphate nanoporous materials for energy storage and peroxide detection†

A. M. Mansour, *[a] Hend S. Magar, [b] Amir Elzwawy, [c] Ali B. Abou Hammad[a] and Amany M. El Nahrawy [a]

The demand for clean, efficient, and sustainable energy storage solutions drives significant advancements in materials science. This study investigates the synthesis and characterization of cadmium zinc phosphates (CdO-ZnO-P_2O_5) doped with different tungsten (CZWP) concentrations using the sol–gel method. The structural, binding energy, morphological, Brunauer–Emmett–Teller (BET) analysis, thermal, optical, and electrochemical properties were thoroughly examined. X-ray diffraction (XRD) confirmed a crystalline structure with tunable properties influenced by tungsten doping. Scanning Electron Microscopy (SEM) revealed well-ordered nanoparticles exhibiting a homogeneous distribution that was enhanced by W doping. BET reveals a moderate specific surface area, mesoporous structure, and dual-porosity characteristics, offering insights into their potential applications in photocatalysis, energy storage, and gas sensing. The TGA results indicate that tungsten doping in cadmium zinc phosphate reduces the material's coordinated water content and increases the thermal stability of the material. Optical analyses demonstrated a shift in the bandgap and an increase in optical electronegativity, highlighting the material's potential in optoelectronics. Electrochemical characterization using cyclic voltammetry (CV) and electrochemical impedance spectroscopy (EIS) identified an optimal doping level of 2.0% W for improved charge transfer and specific capacitance, confirming its suitability for supercapacitors. Furthermore, the 2.0% W-doped electrode exhibited outstanding performance in hydrogen peroxide (H_2O_2) sensing, achieving high sensitivity, a wide linear range, and low detection limits. These findings highlight CZWP nanostructures as promising candidates for energy storage and sensing applications.

Received 20th February 2025
Accepted 2nd May 2025

DOI: 10.1039/d5ra01248a

rsc.li/rsc-advances

1 Introduction

Science is advancing rapidly to tackle energy storage and industrial challenges. Energy acts as the driving force behind the growth of civil society and development. Thus, the acquisition of clean, eco-friendly, and low-cost routes for energy production, storage, and manipulation is immensely required.[1–4] Scientists and engineers are conducting research on energy conversion and storage as a crucial topic due to the rising demand for energy appliances, according to changes in lifestyle and living standards.[5,6] Also, these devices can be deployed in situations where substantial power density is needed, especially for electric cars, electrical apparatus, sensors, supercapacitors, and CO_2 emission mitigation.[7,8] The challenge for these sectors is to optimize a cost-effective approach and achieve a robust active material.[6,9,10]

Amongst the elevation of preparation methodologies, the sol–gel technique is believed to satisfy desired requirements as it offers a facile, reproducible, and consistent route with high purity of the synthesized nanomaterials.[11–13] Besides, the sol–gel requires reduced temperature and provides a low-cost as well as manipulated optical, electrical, and morphological facility.[14–16] Moreover, the mentioned sol–gel procedure is capable of the introduction of binary nanoparticles concurrently delivering a one-pot synthesis track upon mixing two metals or metal oxide precursors in specific adjustable portions.[14,17–20]

It is noteworthy to mention that the introduction of novel materials can reflect an impactful contribution to attaining high-performance supercapacitor strategies.[21] Nanostructured materials are promising according to their elevated

[a]*Solid State Physics Department, Physics Research Institute, National Research Centre, 33 El Bohouth St., Dokki, Giza, 12622, Egypt. E-mail: amamansour@gmail.com; ae.mansour@nrc.sci.eg*

[b]*Applied Organic Chemistry Department, National Research Centre (NRC), 33 El Bohouth St., Dokki, Giza, 12622, Egypt*

[c]*Ceramics Department, Advanced Materials Technology and Mineral Resources Research Institute, National Research Centre (NRC), 33 El Bohouth St., Dokki, Giza, 12622, Egypt*

† Electronic supplementary information (ESI) available. See DOI: https://doi.org/10.1039/d5ra01248a

specifications and provided merits. Nanoparticles are widely used in various applications due to their exceptional properties, including a larger surface area, enhanced structural stability, higher surface energy, and increased diffusion rates.[22,23] An important consideration in energy conversion and storage progress for sustainable human development is specific capacitance, which can be raised by producing electrode materials with superior topologies and structural features.[24] Incorporating the nanoparticles into a composite matrix provides additional non-approachable specifications for the original matrix. The tuning might comprise physical, chemical, and biological advantages. Metal phosphates are an emergent category of materials with enlarged porosity, which awards them a high specific capacity plus ionic conductivity.[21]

Motivated by these points, we explored the former research works for close composites in the energy storage application area. In this context, we have focused on cadmium incorporation with zinc phosphate-based materials and close composites.

R. Ahmed *et al.* have reported on the synthesis of NiO nanorods doped in Cd–Zn to improve their performance in supercapacitors.[7] A maximum capacitance of (1485.19 F g^{-1}) was verified for $Cd_{0.03}Zn_{0.07}NiO$ in their work, plus they attributed a correlation between specific capacitance and optical properties. Galvanostatic charge–discharge (GCD) outcomes grasped superior charging-discharging capability with 82% cyclic retention.[7] Zn doped CdS nanoparticles were introduced earlier through a co-precipitation approach. The authors concluded that the structure exhibits a pseudocapacitive nature and can deliver ~300 F g^{-1} for the specific capacitance.[25] N. Anwar *et al.* have successfully produced composites of polyaniline cadmium oxide (PANI-CdO) through an *in situ* chemical polymerization process. The PANI-5% CdO composite showed a notably high specific capacitance of 866 F g^{-1}.[26] In another report, Cu and Zn-doped CdO were synthesized using the co-precipitation method. Superior optoelectronics with high-performance electrochemical supercapacitor characters were approached.[27,28] The influence of doping Nd^{3+} onto the CdO nanoparticles through a hydrothermal process is delivered. The 652 F g^{-1} specific capacitance was maintained for 3% Nd^{3+} doping with high capacitive retention after 5000 cycles.[24] Binder-free zinc phosphate electrodes were synthesized by a hydrothermal approach, where this structure revealed a negligible charge transfer resistance accompanied by an increased specific capacity.[21]

The investigation of the newly synthesized materials with several functions in different fields, such as sensors[29,30] and supercapacitors, has been considered. Furthermore, the materials with high capacitance and cycling stability for supercapacitor application are used as promising storage energy material.[31–33] Sensitive and reliable sensors for peroxide detection by low-cost and facile methods are important.[34–36] Different analytical techniques are used for peroxide detection, such as electrochemistry, spectrophotometry, and chromatography.[37–39] The advantages of the electrochemical method are sensitivity, selectivity, and simplicity, besides the low-cost.[33,38,40–44] Sensors are the best tool for accurate,[45,46] fast, and sensitive detection of biological samples,[47,48] drugs, and diseases to diagnose.[49,50] The use of nanomaterials modified screen-printed electrode surface advantage of electrochemical sensors properties.[51,52] So, it is important to modify the surface of the electrode with new materials that have high electrocatalytic properties to produce highly sensitive electrochemical sensor platform(s).

In a former effort in our group, we successfully prepared cadmium zinc nickel phosphates through a sol–gel spin coating process. That work demonstrated the structure's enhanced optoelectronic and morphological features.[53] This work uses a combination of phosphorus (P) as a based former in the CZP structure, contributing to electronic structure, crystallinity, and improved electrochemical properties. Additionally, both cadmium and zinc offer excellent semiconducting properties, good optical behavior, and stable electron transfer matrices. Tungsten (W) helps enhance electrochemical performance and fine-tunes the optical band gap. This multi-ion approach results in nanostructures with superior performance for supercapacitors and H_2O_2 detection applications.

Despite the extensive research on energy storage materials and biosensors, there remains a critical need for materials that can deliver high specific capacitance, efficient electron transfer, and enhanced sensing capabilities. Current materials often face challenges such as limited surface area, poor conductivity, and insufficient sensitivity. This study addresses the tungsten-doped cadmium zinc phosphate (CZWP) nanostructure that combines superior electrochemical performance with high sensitivity for hydrogen peroxide detection. In our current work, we have prepared the cadmium zinc phosphates CdO-ZnO-W-P_2O_5 (CZWP) nanoparticles through the sol–gel route, while the doping of Tungsten was delivered with different ratios. The structural, morphological, optical, and electrochemical specifications of the microstructure were thoroughly investigated. This system is a semiconductor with high conductivity despite the existence of the phosphate. This novel structure is not explored in a former report for energy storage areas, and hence, the attained results validate the promising potentials for optoelectronics, energy storage, sensors, and related applications.

2 Experimental work

2.1. Materials

All chemicals were purchased from Sigma and used without further purification. Triethyl phosphate, cadmium nitrate (CdN_2O_6), zinc acetate ($C_4H_6O_4Zn$), tungsten nitrate ($W_3C_3H_{11}IN_3O_6$), and hydrochloric acid were used in the experiments, and the solutions were prepared using distilled water.

2.2. Cadmium zinc phosphates doped with tungsten (CZWP) nanoporous preparation

Employing an advanced sol–gel process, we undertook the preparation of CZWP nanopowders under standard ambient conditions. We prepared CZWP nanopowders using an advanced sol–gel process under standard ambient conditions. First, we prepared an acid solution by diluting 15 mL of (35%) hydrochloric acid (HCl) with 45 mL of distilled water. Next, we

meticulously prepared individual precursor solutions of CZP-based zinc, phosphorus, and cadmium precursors, dissolving each salt in a solution of H_2O and HCl. Then, we combined the cadmium and zinc salt solutions and stirred them magnetically for one hour. The required amount of triethyl phosphate was added to 20 mL of absolute ethanol while stirring, followed by the addition of cadmium zinc solution to the P_2O_5 solution under vigorous magnetic stirring to form the CZP-based composite.

For the W samples, start by mixing the evaluated weight of tungsten nitride (sigma) with 50 mL of H_2O, 20 mL of C_2H_5OH, and 5 mL of HCl to create the activated tungsten solution. Then, add W sol to the cadmium zinc solution before mixing with phosphorus-based, and stir magnetically for one hour. After mixing, let the resulting solution mature overnight in ambient air. Finally, dry at 200 °C for 10 hours, followed by calcination of the prepared xerogel at a temperature of 600 °C for 3 hours. The nanopowder samples were gradually cooled to room temperature inside the furnace to allow the nanoparticles to form well-ordered and crystalline nanopowder. A schematic diagram of materials synthesis process is presented in Fig. 1.

2.3. Characterization techniques

For the structural analysis of CZWP nanoparticles, we utilized a (D8-Bruker Advance) X-ray diffractometer equipped with Cu Kα radiation, operating at 40 kV and 40 mA. This instrument facilitated the exploration of crystal structure by scanning the samples in the 2θ range of 10–70° with a step size of 0.05°.

For SEM-EDX analysis, CZP and CZWP samples were ground before being loaded on a copper sheet. To observe the morphology of nanopores at high resolution, we employed SEM (Quanta FEG-250: 20 kV), integrated with an Energy Dispersive Spectroscope (EDX). This technique offered detailed imaging of the nanoparticle surface and structure.

The samples' surface area, pore size, and particle distribution were analyzed *via* nitrogen adsorption–desorption isotherms using a NOVA 2000 analyzer (Chromatic, UK) at 77 K. Prior to this, samples were degassed at 150 °C under vacuum for 6 hours. The specific surface areas were calculated using the BET method, and pore-size distributions were obtained *via* the NLDFT method. Total pore volume was determined from the maximum relative pressure adsorption. Hydrogen content analysis was conducted using PCI curves, measured volumetrically with the AMC PCI-HP 1200. A 0.5 g sample was degassed at 200 °C for 2 hours at 0.01 bar, cooled to 77 K, and exposed to hydrogen pressures up to 20 bar. Measurements were recorded automatically, with temperature controlled to ±0.1 °C and hydrogen content accuracy within ±0.04 wt%.

The thermal behavior was characterized through thermogravimetric analysis (TGA) using an SDT-Q600 instrument (USA), conducted under a nitrogen atmosphere with a heating rate of 10 °C per minute over a temperature range of approximately 25 °C to 800 °C.

To study the optical properties of the nanopowders across a wide wavelength range (190 to 2500 nm), we utilized a JASCO model V-570 UV-Vis-NIR spectrophotometer. This technique allowed us to obtain diffused reflectance spectra, providing

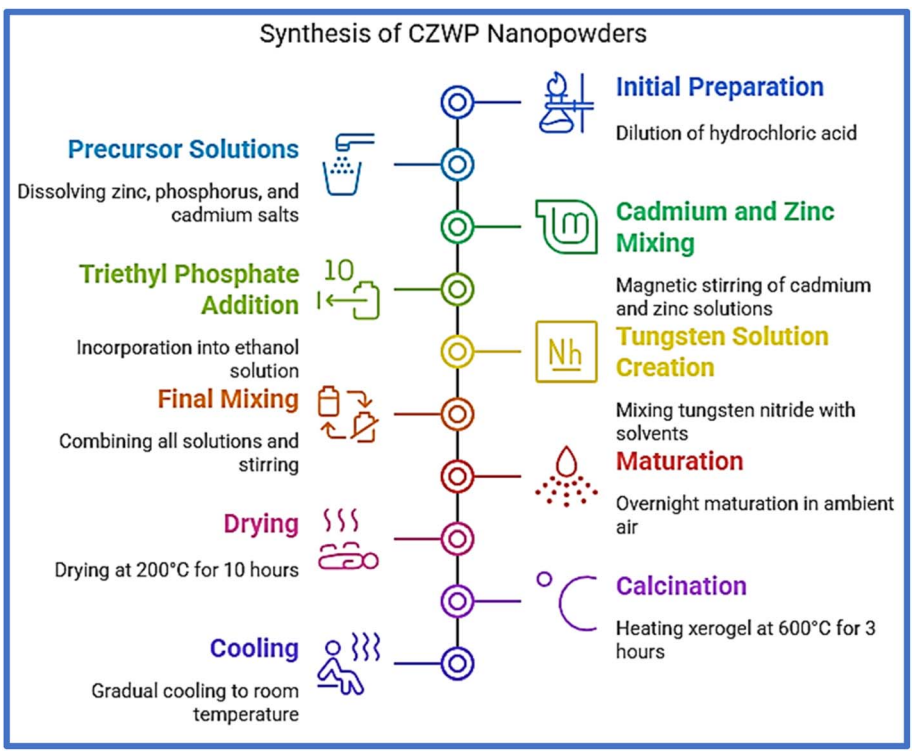

Fig. 1 Schematic diagram of materials synthesis process.

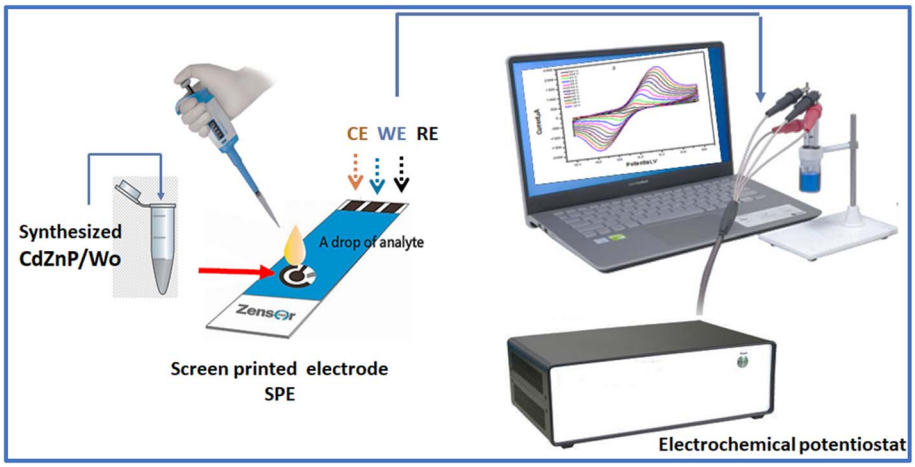

Fig. 2 The modified SPE preparation and electrochemical detection methods.

insights into the optical behavior of the CZWP nanopowders. The diffuse reflectance (DR) mode relies on both scattering and absorption coefficients to analyze the optical properties of the samples. In this study, we utilized DR spectroscopy to examine the UV-Vis-NIR absorption properties of the pure and doped CZWP nanopowders.

X-ray photoelectron spectroscopic (XPS) examine was carried out by a Thermo-ESCALAB 250 instrument.

The used materials are potassium chloride, potassium ferricyanide and potassium ferrocyanide, potassium mono/dihydrogen phosphate, hydrogen peroxide, sodium hydroxide (NaOH), and hydrochloric acid (HCl) from sigma Aldrich.

Electrochemical experiments were carried out using an electrochemical workstation CS350H potentiostat/Galvanostat and CHI-potentiates and screen-printed electrodes (SPEs).

For SPE modification stepwise, weigh 10 mg of the synthesized materials added to 1 mL distilled water in Eppendorf, and sonicate for 30 min up to obtaining a homogenous suspended solution. Then, take 10 μl of the suspended solution and dropwise on the surface of the screen-printed electrode, and left to dry. CV and EIS measurements were carried out in a mixture solution of 0.1 M KCl and 0.005 M of the ferro/ferri cyanide $[Fe(CN)_6]^{3-/4-}$ (see Fig. 2).

3 Results and discussion

3.1. XRD assessment

Fig. 3 reveals the structural behavior of the synthesized CdO-ZnO-W-P_2O_5 (W-CdZnP), while an increasing tungsten (W) content is demonstrated. The diffraction patterns span a wide range till a diffraction angle of 70°. The noticeable diffraction peaks exist around 20–40°. The apparent diffractograms reveal the repeated and ordered arrangement of the atoms as a crystalline phase of the structure. The correlated planes with the diffraction angles for the highest intensity peaks are located at 2θ of 19.02, 23.34, 25.19, 29.9, 34.55, 37.4, 38.41, 41.77, 46.28, 55.5, 58.7 and 58.8 which are attributed to the (110), (200), (−113), (−114), (022), (−3−11), (115), (−224), (−404), (123), (226), and (−319) JCPDS file No. 00-011-0035.[54] The strongest peaks were observed in W-doped samples (2θ = 22° to 33°), confirming that W reinforces the internal structure of CdZnP.

The slight discrepancy of the positions might be due to the rising dislocations and unit cell variation upon the inclusion of

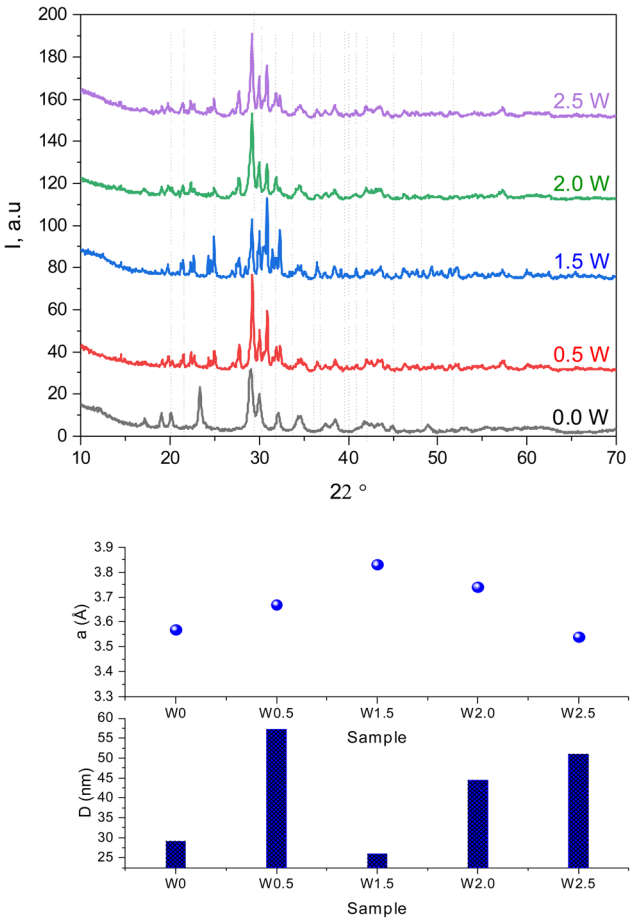

Fig. 3 The XRD of CdO-ZnO-W-P_2O_5 (CZWP) showing different doping wt% of W in the structure (up), and the lattice parameter dimensions with the crystallite size depiction (down).

composition constitutes due to atomic radii variations and to the rotation of some crystalline grains during the preparation processes (Cd radius is around 0.95 Å (ref. 55 and 56)). Furthermore, few parameters can be extracted from the plotted pattern. Degree of crystallinity is influenced by the hardness degree, heat resistance, and the stiffness. The crystalline nature and the degree of crystallinity (X_c) might be determined upon considering the area under the crystalline peaks and other peaks. This value is governed as per the subsequent equation[57]

$$(X_c\text{cryst. degree}) = \left\{\frac{\text{area}_c}{\text{area}_{all}}\right\} \quad (1)$$

Upon the introduction of the W into the structure, an accompanying dislocation density might arise due to the variation in the effective atomic radius of the elements as well as the unit cell. Dislocations are a critical characteristic that impacts a material's electrical performance.[58] The occurring dislocation density (δ) is inversely related to the crystallite size as[59,60]

$$(\delta) = D^{-2} \quad (2)$$

The average size of crystallites from which the grains are formed are estimated based on the highest intense peak, according to the Scherrer equation[61]

$$D = (\kappa\lambda)/(\beta\cos\theta) \quad (3)$$

κ and λ refer to the shape factor, which is approximately 0.9, and the incident X-ray wavelength, respectively. Besides, β, θ represents the full width at half intensity of the peak and Bragg's diffraction angle, respectively. It is noteworthy to mention that the height of the peak is correlated with the domain size. Existing atoms in the crystal separately behave as a light source similar to the slits in a grating, hence any reduction in the domain size pursues less atoms residence in the crystal, subsequently fewer spots as well as peak intensity.[61]

The lattice parameter might be calculated upon considering the miller indices values and the interplanar d-spacing, wavelength, and diffraction angle as:[62,63]

$$a = \left\{\frac{\lambda}{2\sin\theta}\left(h^2 + k^2 + l^2\right)^{1/2}\right\} \quad (4)$$

Another approach that might be trusted for the acquisition of the crystallite size along with the uprising strain parameters is the Williamson–Hall plot.[64,65] Generally, the broadening of the diffraction peaks occurs as an outcome of the crystallites broadening (β_D), and the lattice strain broadening (β_S). The overall sum of the broadening is mathematically represented as:[66,67]

$$\beta_{tot.} = \beta_D + \beta_S = \left[\frac{\kappa\lambda}{D\cos\theta}\right] + 4\varepsilon\tan\theta \quad (5)$$

This equation, following arrangement, is rewritten in the form of a straight-line equation ($y = Ax \pm C$) represented as:

$$\beta_{tot.}\cos\theta = \left[\frac{\kappa\lambda}{D}\right] + 4\varepsilon\sin\theta \quad (6)$$

This line indicates either a positive or negative slope, with the negative slope representing intrinsic compressive strain (Fig. 4). In contrast, the positive slope is associated with the presence of tensile strain.[58,68,69] The strain can be determined from the straight-line slope and compared to an alternative method of calculating the strain (Table 1).[70]

$$\varepsilon = \beta_S/(4\tan\theta). \quad (7)$$

Furthermore, the crystallite size is determined by finding the intercept where:

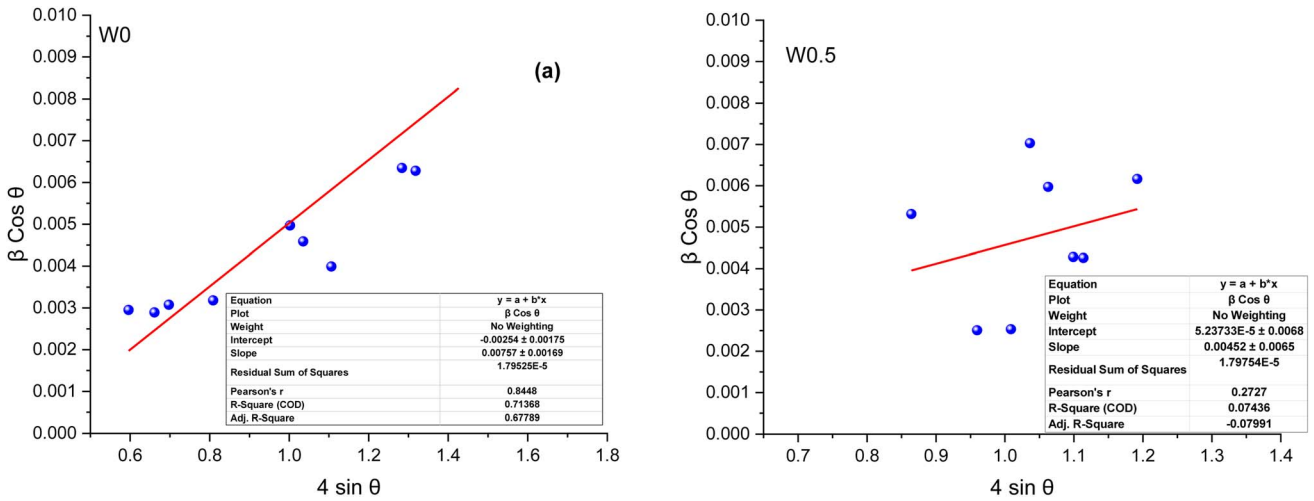

Fig. 4 The relation between $\beta\cos\theta$ and $4\sin\theta$, at where the crystallite size and microstrain are seized from the slope and intercept, familiarly denoted as Williamson–Hall plot.

Table 1 Tabulated parameters derived from the XRD pattern

Sample	D (nm)	D (W–H)	δ (nm^{-2})	ε	ε (W–H)	d-spacing (Å)	a (Å)
0.0 W	29.16	108	0.001176	−0.02871	0.00757	3.07453	3.57
0.5 W	57.19	—	0.000306	−0.01897	0.00452	3.05475	3.67
1.5 W	26.02	—	0.001477	−0.28835	—	2.89547	3.83
2.0 W	44.44	—	0.000506	−0.02297	—	3.05967	3.74
2.5 W	51.05	—	0.000384	−0.01994	—	3.05986	3.54

$$D = \frac{\kappa\lambda}{\text{intercept(with } y\text{-axis)}} \quad (8)$$

3.2. XPS study

XPS attained the chemical analysis of CZP doped with 2.5 W nanoparticles (Fig. 3), which agreed with the evaluated cadmium zinc phosphates (CdO-ZnO-W-P_2O_5, CZWP) doped with 2.5 W composition. Fig. 5 shows the general survey spectra of CZP-W nanoparticles.

XPS studies of nanoparticles CZP and CZP-W are of particular interest because XPS has the unprecedented capability to reveal insights into electronic structure modification owing to diverse cases of doping and defects in CZPO-based nanoparticles.[71,72] This means that the CZP and CZWP compositions and nominals are well-matched. The binding energies of 409.71 eV in the $3d_{5/2}$ state and 416.71 eV in the $3d_{3/2}$ state matched cadmium, which agree well with the 6.7 eV spin–orbit energy splitting between the Cd $3d_{5/2}$ and $3d_{3/2}$ states and agree with previous reports.[73,74] The Zn $2p_{3/2}$ (1023.7 eV) and Zn $2p_{1/2}$ (1046.8 eV) peaks, respectively, are shifted to higher energy by adding W (1029.7 eV and 1054.71 eV). The Zn peaks change with the addition of 2.5 W because the electronegativity of W is higher than both Cd, Zn, and P, which indicates that the W ions have loaded into the CZP lattice.[75,76] The peak at 504.8 eV, reported for interstitial zinc (Zni) attributed to the interstitial (Zn–O) bonds in binding energy 490–505 eV.[77] Additionally, the peak at 985.7 eV, corresponding to another Zn LMM Auger transition, further supports the presence of Cd^{2+} ions within the CZP structure.[71,75]

O 1s (CZP) showed a binding energy peak at 534.79 eV, which shifted to 536.71 eV with adding 2.5 W. This represents the metal–O peaks for CZP and surface-adsorbed oxygen species, respectively.[78–80] Additionally, the binding energies at around 14.7, 92.69, 193, and 235.3 eV can be attributed to zinc-oxygen and metal–oxygen (M–O) bonds.[77] All binding energies for CZP and CZP-2.5 W are corrected using the C 1 s peak (JEOL reference for C 1s binding energy) at 284.2 eV, which shifted to 288.4 eV during peak fitting.[81,82] The peak detected at ~495 eV is ascribed to the Zn-LMM (Auger transition), while the one at ~623 eV likely rises from the relaxation of electrons linked with Cd^{2+} (3d).[72,83] Also, our XPS results for oxygen and phosphorus (P_2O_5) match with previously reported findings. Wang *et al.* reported that, the O 1s peaks are observed around 532.51 eV and 534.0 eV, while the P $2p_{3/2}$ peak appears at 135.0 eV for phosphorus pentoxide, where the oxidation state of phosphorus is +5.[81]

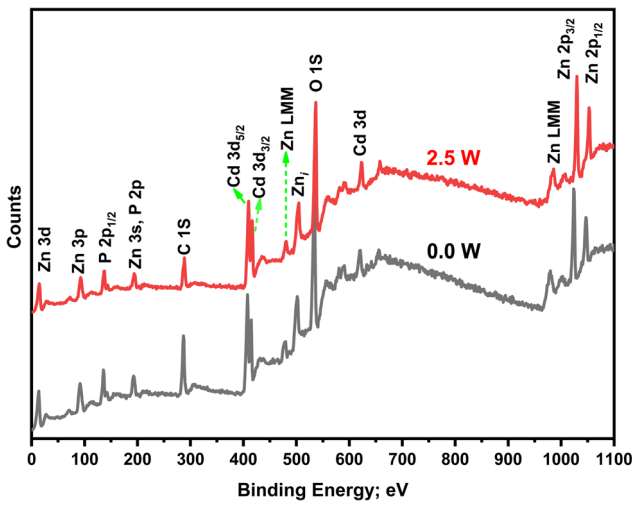

Fig. 5 XPS spectra of CZP and doped with 2.5 W nanoparticles.

3.3. SEM

The surface characteristics of nanoparticles CZP, both in its pure form and doped with 2.5 mol% WO, are depicted in Fig. 6a and b. Initially, the nanoparticle structures calcined at 600 °C, revealing a notably high density of nanoparticles for both the pure and Wo-doped samples, as illustrated in Fig. 3. The density of these nanospheres experienced an increase with the incorporation of W. Furthermore, the presence of W led to the formation of CZP/Wo structures with a nanoparticle's morphology, featuring a denser nanostructure, as depicted in Fig. 3b. SEM imaging elucidates the fine nanoparticles with some agglomerated nanoparticles morphology of the CdZn-phosphate material, offering consistently well-defined nanostructures. The surface morphology indicates a homogeneous particle distribution and stresses the precision of the controlled synthesis process. The introduction of tungsten through doping may induce variations in size or aggregation patterns, consequently influencing the overall size distribution of these nanostructures. Fig. 6c displays the EDX spectrum of the phosphorous cadmium zinc tungsten (CdZnP/2.5 WO) in which the attendance of all elements such as P, Zn, Cd, O, and W are confirmed. Thus, the EDX study confirms the active doping of W in CdZnP nanoparticles.

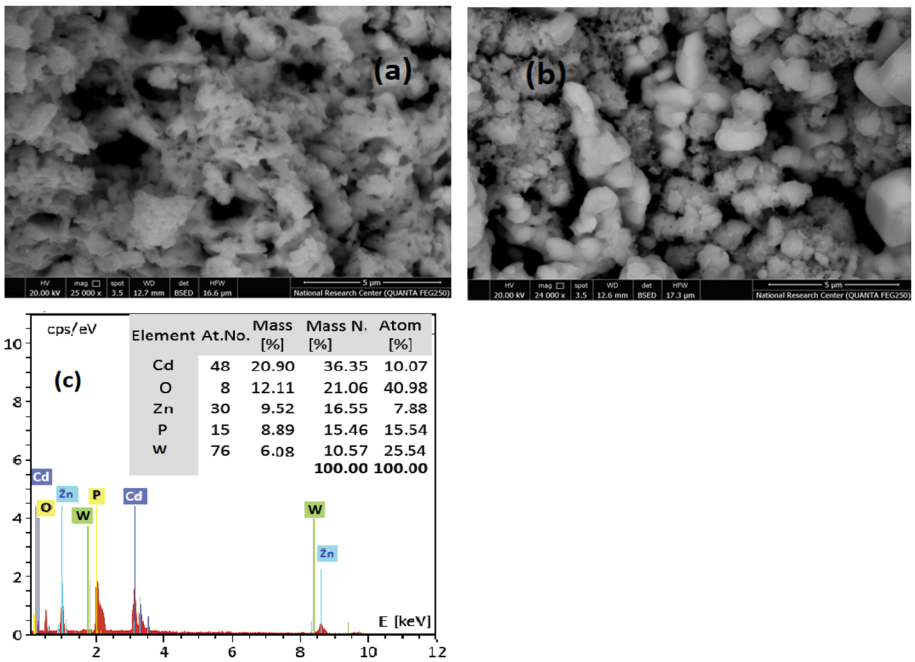

Fig. 6 SEM morphology of: (a) undoped CdZn-phosphate nanoporous, (b) CdZn-phosphate doped 2.5 mol% W, and (c) the particle distribution.

3.4. Brunauer–Emmett–Teller (BET) analysis

The Brunauer–Emmett–Teller (BET) analysis is a widely used technique to determine the specific surface area, pore size distribution, and porosity of materials.[84] In this study, the BET analysis was conducted on cadmium zinc phosphides (CdZnPs), a class of semiconducting materials with potential applications in optoelectronics, photocatalysis, and energy storage. The results provide critical insights into the material's structural properties, which are essential for understanding its performance in various applications.

The BET-specific surface area of the cadmium zinc phosphides was determined to be 7.2577 $m^2 g^{-1}$. This value indicates a moderate surface area, which is typical for crystalline semiconductor materials. A higher surface area would be desirable for applications such as catalysis or gas sensing, where active surface sites play a critical role.[85] The relatively low surface area suggests that the material may have limited porosity, which could influence its adsorption capacity and reactivity.

The total pore volume was calculated to be 7.3461×10^{-3} $cm^3 g^{-1}$, with a mean pore diameter of 4.0487 nm. According to the IUPAC classification, these findings classify the material as mesoporous, as the pore sizes fall within the range of 2–50 nm.

The BJH (Barrett–Joyner–Halenda) plot (Fig. 7a), derived from the adsorption branch, confirms the presence of mesopores. The peak pore diameter observed in the pore size distribution analysis was 3.92 nm, consistent with the mean pore diameter. The material's mesoporous nature could enhance its utility in applications requiring efficient mass transport, such as battery electrodes or photocatalytic systems.[86]

The adsorption/desorption isotherm reveals a type IV isotherm with a hysteresis loop, characteristic of mesoporous materials. The hysteresis loop (Fig. 7b) indicates capillary condensation occurring within the mesopores, further corroborating the pore size distribution results. The relative pressure (p/p_0) at which the hysteresis loop occurs provides additional evidence of the mesoporous structure, as it typically appears in the range of 0.4–0.9 for such materials.

Advanced pore size distribution analysis using NLDFT/GCMC (Grand Canonical Monte Carlo) simulations (Fig. 7c) confirmed the presence of slit-shaped pores with a peak pore diameter of 10.383 nm. This discrepancy between the BJH and NLDFT results highlights the importance of using complementary techniques to accurately characterize complex porous structures.[87]

The BET-specific surface area of the tungsten-doped cadmium zinc phosphides was determined to be 15.635 $m^2 g^{-1}$, significantly higher than the undoped counterpart (7.2577 $m^2 g^{-1}$). This increase suggests that tungsten doping enhances the material's surface area, potentially by creating additional active sites or altering the morphology during synthesis. A higher surface area is advantageous for applications such as catalysis, where increased surface exposure facilitates enhanced reactivity.[85] The total pore volume was calculated to be 1.5104×10^{-2} $cm^3 g^{-1}$, with a mean pore diameter of 3.8640 nm. These findings classify the material as mesoporous, consistent with the IUPAC classification for pores within the range of 2–50 nm.

The BJH (Barrett–Joyner–Halenda) plot (Fig. 8a) derived from the adsorption branch confirms the presence of mesopores, with a peak pore diameter of 3.92 nm. This value aligns closely with the mean pore diameter, indicating a relatively uniform pore structure.

The adsorption/desorption isotherm exhibits a type IV isotherm with a hysteresis loop (Fig. 8b), characteristic of mesoporous materials. The hysteresis loop occurs at relative

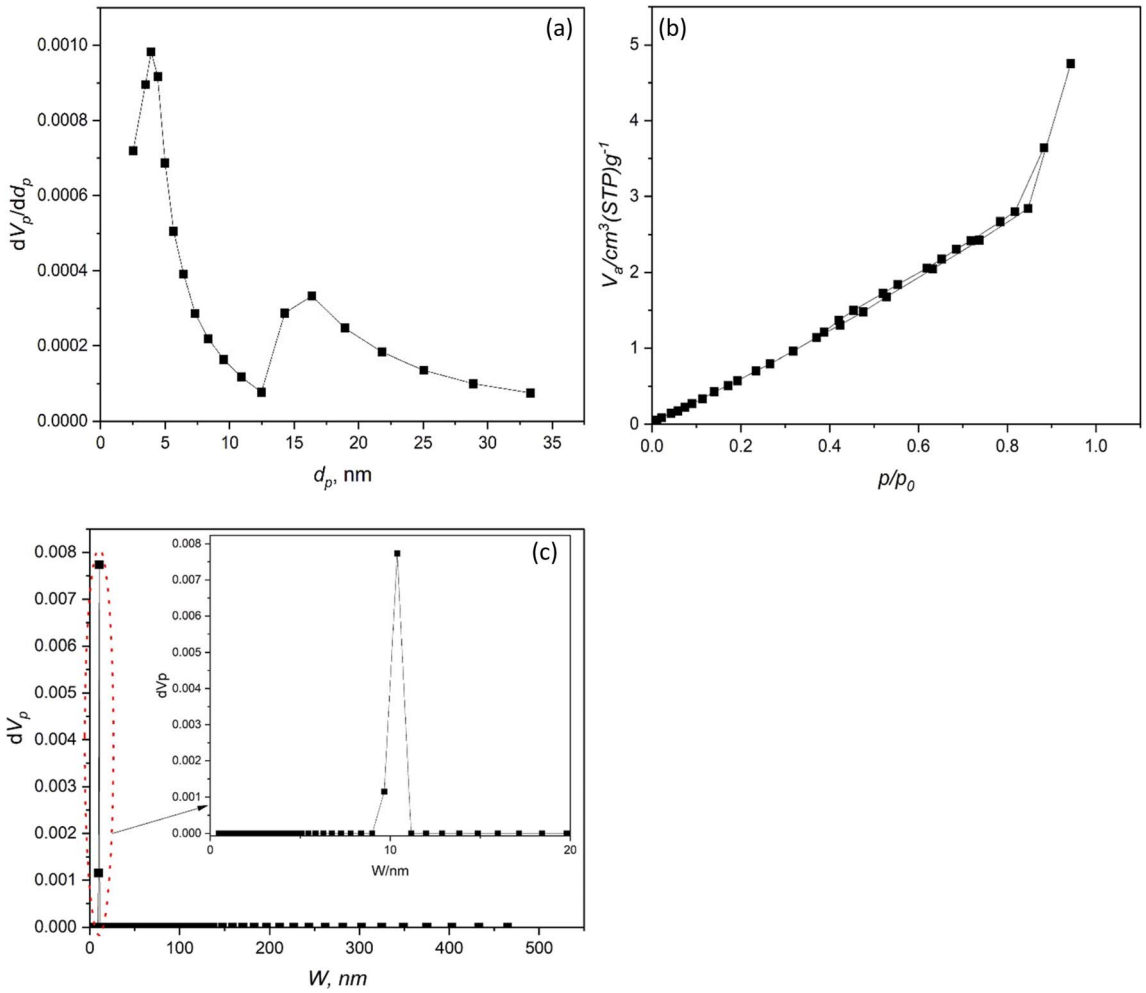

Fig. 7 CZP (a) BJH pore size distribution plot with a peak pore diameter of 3.92 nm, (b) adsorption/desorption isotherm showing type IV behavior with a hysteresis loop, (c) NLDFT pore size distribution analysis revealing dual-porosity with peaks at 10.383 nm.

pressures (p/p_0) between 0.4 and 0.9, indicating capillary condensation within the mesopores. The shape of the isotherm further supports the mesoporous nature of the material and highlights its suitability for applications requiring efficient mass transport.[87] Advanced pore size distribution analysis using NLDFT/GCMC simulations (Fig. 8c) revealed a slit-shaped pore structure with a peak pore diameter of 0.7305 nm.

For the two samples (*i.e.* Pure CZPO and W/CZPO), a smaller pore diameter of about 0.3400 nm was identified, suggesting the coexistence of micropores within the material.[85–87] The dual-porosity structure—comprising both micro- and mesopores—enhances the material's overall surface area and adsorption capacity, making it promising for applications in gas storage and separation.[85–87]

The high vacuum level achieved before measurement (2.778×10^{-4} Pa) ensured the removal of physisorbed species, minimizing interference during analysis. This step is crucial for obtaining reliable BET results, particularly for materials with low surface areas like pure and tungsten-doped CdZnPs. The moderate surface area and mesoporous structure of the studied materials suggest their suitability for applications requiring controlled diffusion and surface interactions.[85–87] For instance, photocatalysis (the mesoporous structure can facilitate efficient light absorption and charge transport, enhancing photocatalytic activity), energy storage (the dual-porosity structure could improve electrolyte penetration and ion diffusion, making the material promising for use in supercapacitors or lithium-ion batteries), and gas sensing (the presence of both micro- and mesopores could enhance the material's sensitivity to target gases by providing abundant active sites).

3.5. Thermogravimetric analysis (TGA)

The provided thermogravimetric analysis (TGA) curves (Fig. 9) show the weight loss profiles of pure cadmium zinc phosphate (0.0 W) and tungsten-doped cadmium zinc phosphate (2.5 W) as a function of temperature. The analysis reveals critical insights into the thermal stability, dehydration behavior, and structural changes in these materials.

Both samples exhibit significant weight loss in the range of 55–185 °C. The pure sample (0.0 W) loses 2.7% of its initial weight, while the tungsten-doped sample (2.5 W) loses 1.75%. This weight loss is attributed to the release of crystal water

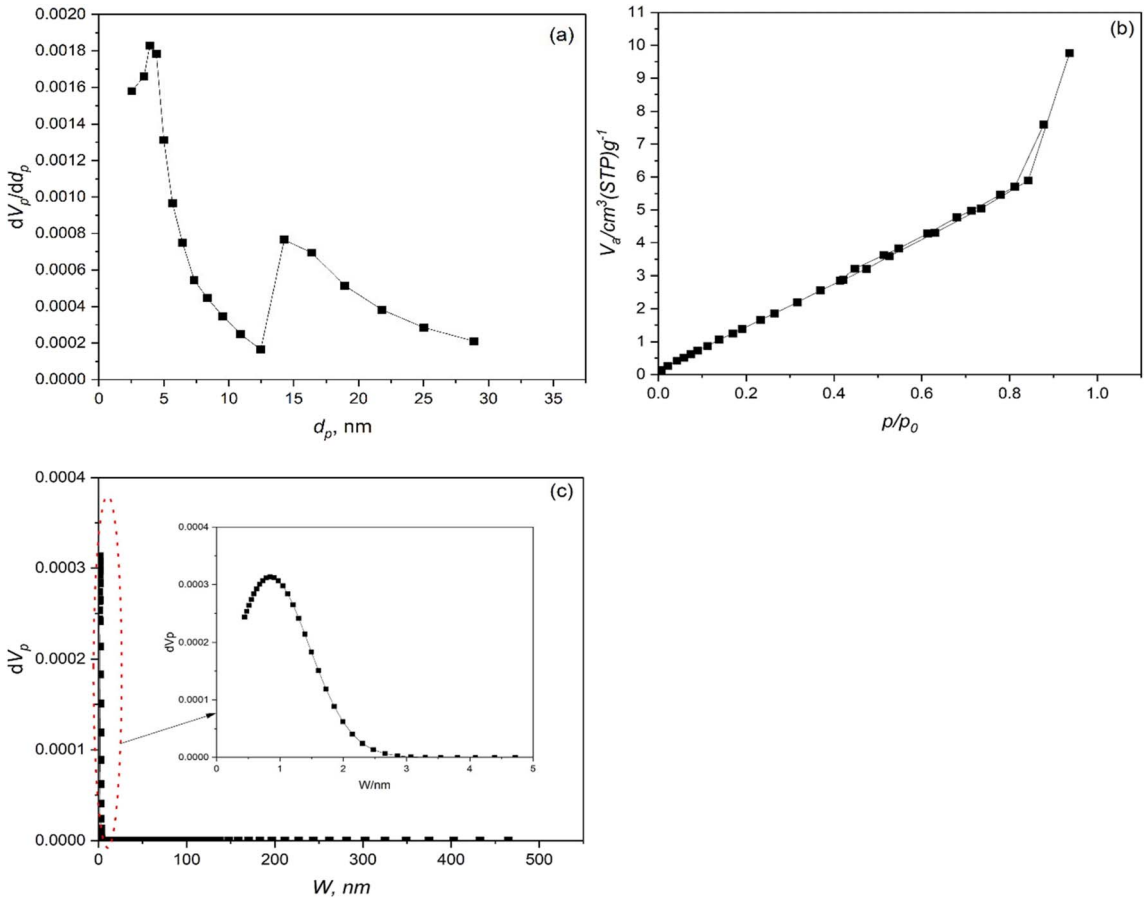

Fig. 8 W doped CZP (a) BJH pore size distribution plot with a peak pore diameter of 3.8640 nm, (b) adsorption/desorption isotherm showing type IV behavior with a hysteresis loop, (c) NLDFT pore size distribution analysis revealing dual-porosity with peaks at 0.7305 nm.

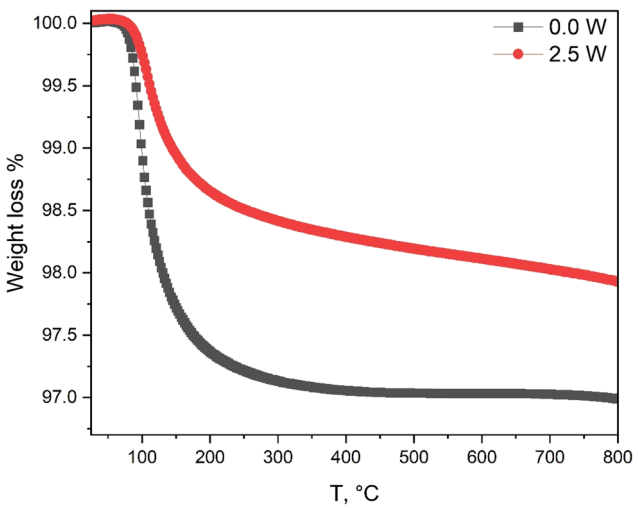

Fig. 9 The TGA curves of 0.0 W and 2.5 W samples.

molecules that are coordinated within the crystal lattice of the phosphates.[88,89] Such water molecules are typically weakly bonded and are thermally labile, meaning they can be easily removed upon heating.

The difference in weight loss between the two samples (2.7% *vs.* 1.75%) suggests that doping with tungsten affects the hydration state of the material.[90] Specifically, the lower weight loss in the doped sample indicates that tungsten incorporation may reduce the number of available sites for water coordination or alter the bonding strength of the water molecules.[91]

Above 200 °C, both samples reach a plateau in their weight loss curves, indicating that the crystal water has been completely removed, and the materials exist in an anhydrous state. The plateau signifies that all thermally labile water molecules have been expelled from the crystal lattice.[92] This transition temperature (around 200 °C) is characteristic of many hydrated phosphates and confirms the completion of the dehydration process.[93]

The slight difference in the onset of the plateau between the two samples (slightly earlier for the doped sample) suggests that tungsten doping may slightly enhance the thermal stability of the crystal structure, potentially due to improved lattice packing or altered interatomic interactions.[94,95] Doping with tungsten can introduce additional electronic and steric effects that stabilize the crystal lattice, thereby delaying further decomposition processes.[94] This stabilization could explain why the doped sample exhibits a more gradual weight loss curve compared to the pure sample.[95]

Beyond 200 °C, both samples continue to exhibit minor weight loss, although at a much slower rate compared to the initial dehydration stage.[93] The doped sample shows a slightly lower overall weight loss compared to the pure sample, which could indicate enhanced thermal stability imparted by tungsten doping.[95] This is consistent with the idea that dopants can improve the structural integrity of host lattices by introducing defects or modifying the electronic structure.[94]

3.6. Optical properties

The optical band gap, a foundational aspect of semiconductors and insulators, delineates the energy distinction between occupied and unoccupied molecular orbitals.[96] It serves as a cornerstone in understanding the electronic and optical characteristics of materials. Techniques such as UV-vis spectroscopy and photoluminescence spectroscopy serve as indispensable tools in determining this crucial parameter. Moreover, in nanosized oxides, optical absorption undergoes intricate changes due to discrete light absorption and size-related quantum phenomena, thereby influencing diffused reflectance through particle size-dependent light scattering.[97]

Employing UV-vis DR (R_D) analysis, a thorough examination of the optical features of the prepared nanocomposites was conducted within the 190–2500 nm (Fig. 10a). The findings delineated the DR behavior: a reflectance peak at 222 nm for a pure sample and shifted to 226 nm by tungsten (W) addition as shown in Fig. 10a inset. There is also a shoulder at 273 nm for all samples. The introduction of W suddenly increases the R_D and then reduces it by more addition in a wavelength range of 190–400 nm. In a higher wavelength, the RD increases by addition W till 1.5 wt% and then decreases by more addition. Notably, the scattering pattern closely aligns with wavelength and W content changes, Fig. 10b and b inset. The introduction and varying concentration of W in CZP-based nanoporous influence the DR by changing the electronic states, forming new scattering centers, and affecting the material's microstructure. The initial increase in DR is due to enhanced scattering from

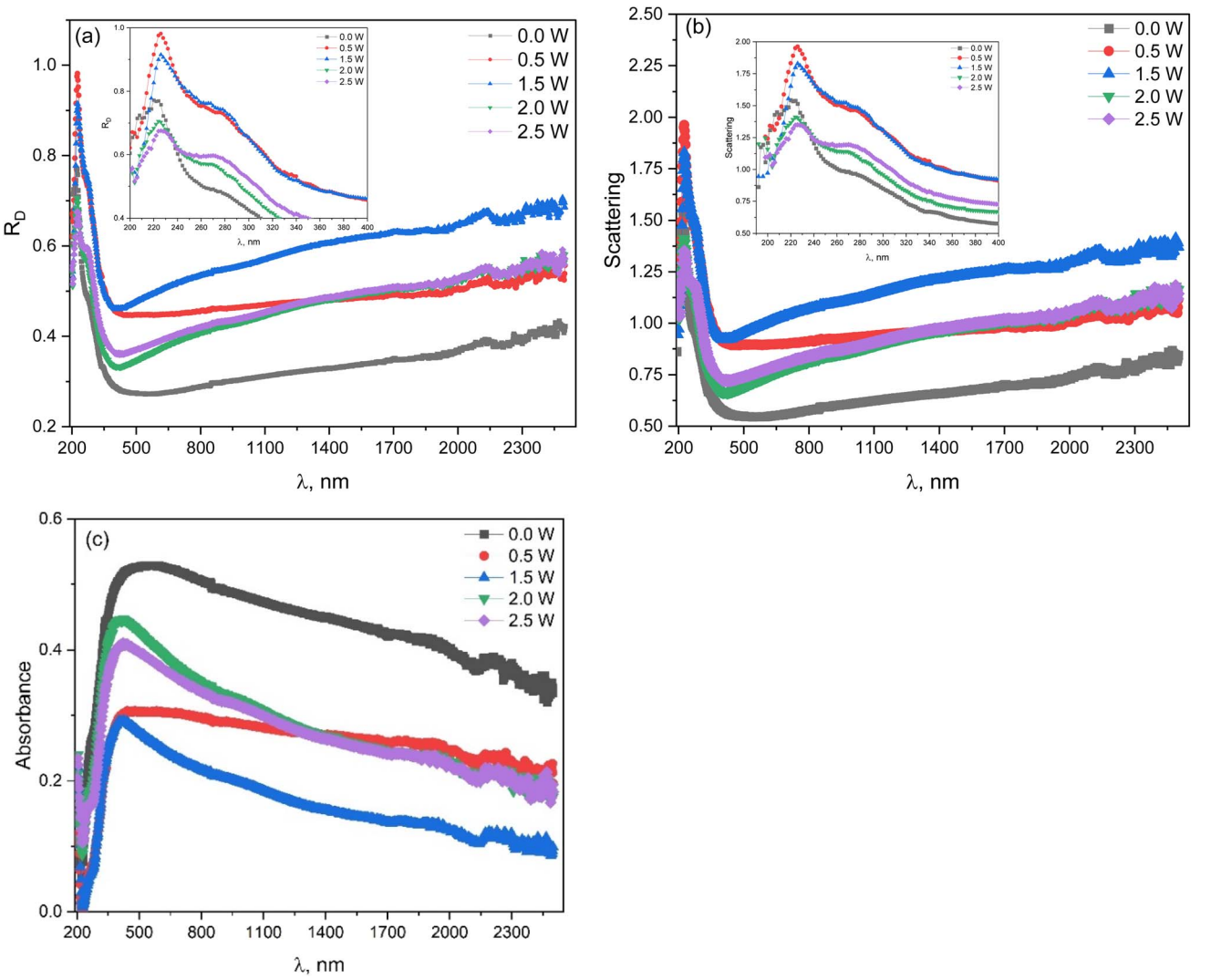

Fig. 10 The wavelength dependence of (a) DR, (b) the scattering, and (c) the wavelength dependence of absorbance of W-doped CZP nanoparticles.

new electronic states, while the subsequent decrease is likely due to the formation of large agglomerates or non-radiative recombination centers that reduce effective scattering.[98,99] The behavior at higher wavelengths further underscores the complex interactions between W ions and the CZP structure.

Fig. 10c provides a comprehensive overview of the wavelength-dependent absorbance changes for different W doping levels. The distinct peak at 541 nm corresponds to a pure sample, and it is related to the transitions associated with the CZP ions and/or their ligands.[100] With W addition, there is a shift of the absorption peak to 420 nm for all samples where this peak offers a $^2B_{2g} \rightarrow {}^2B_{1g}$ ($d_{xy} \rightarrow d_{x^2-y^2}$) transition of tungsten ions.[101] The shift of the absorption edges with increasing dopant concentration is because the addition of W^{6+} ions into Zn^{2+} sites affect the electronic band structure of the material.[102] The shift primarily results from two factors: the Burstein–Moss shift, responsible for broadening the optical band gap, and carrier interactions, inducing a many-body effect that leads to a reduction in the band gap.[102]

Optical absorption, expressed by the Kubelka–Munk formula:[103] $h\nu F(R_\infty) = c(h\nu - E_g)^n$, incorporates (R_∞) as the Kubelka–Munk function, $h\nu$ as photon energy, E_g as the optical band gap, and n as an index (1/2 for direct allowed, 2 for indirect allowed, 3 for direct forbidden, and 3/2 for indirect forbidden).[104] Band identification involves extending the linear Tauc plot or analyzing maxima in the derivative spectra through the absorbance first derivative concerning photon energy.[3]

Fig. 11a and b displays plots of $h\nu \cdot F(R_\infty)^{1/2}$ and $h\nu \cdot F(R_\infty)^2$ against $h\nu$ for gap transition analysis. Direct transition and indirect transition gap types are evident, with the direct transition exhibiting a higher value, which makes an indirect case a more probable case.[105] The increase in indirect transition energy with increasing W content is depicted in Fig. 11c, attributed to the gradual increase in the concentration of W ions and decrease of Cd and Zn ions[106] where the values of E_g align consistently with reported values by.[107,108] This observation is interpreted by Chung *et al.*,[109] who assert that the decrease in CdO content leads to a decrease in non-bridging oxygens, and this led to an increase of band gap.

Semiconductors exhibit a demonstrable correlation between the increase in energy gap and the corresponding decrease in refractive index. Various empirical and semiempirical

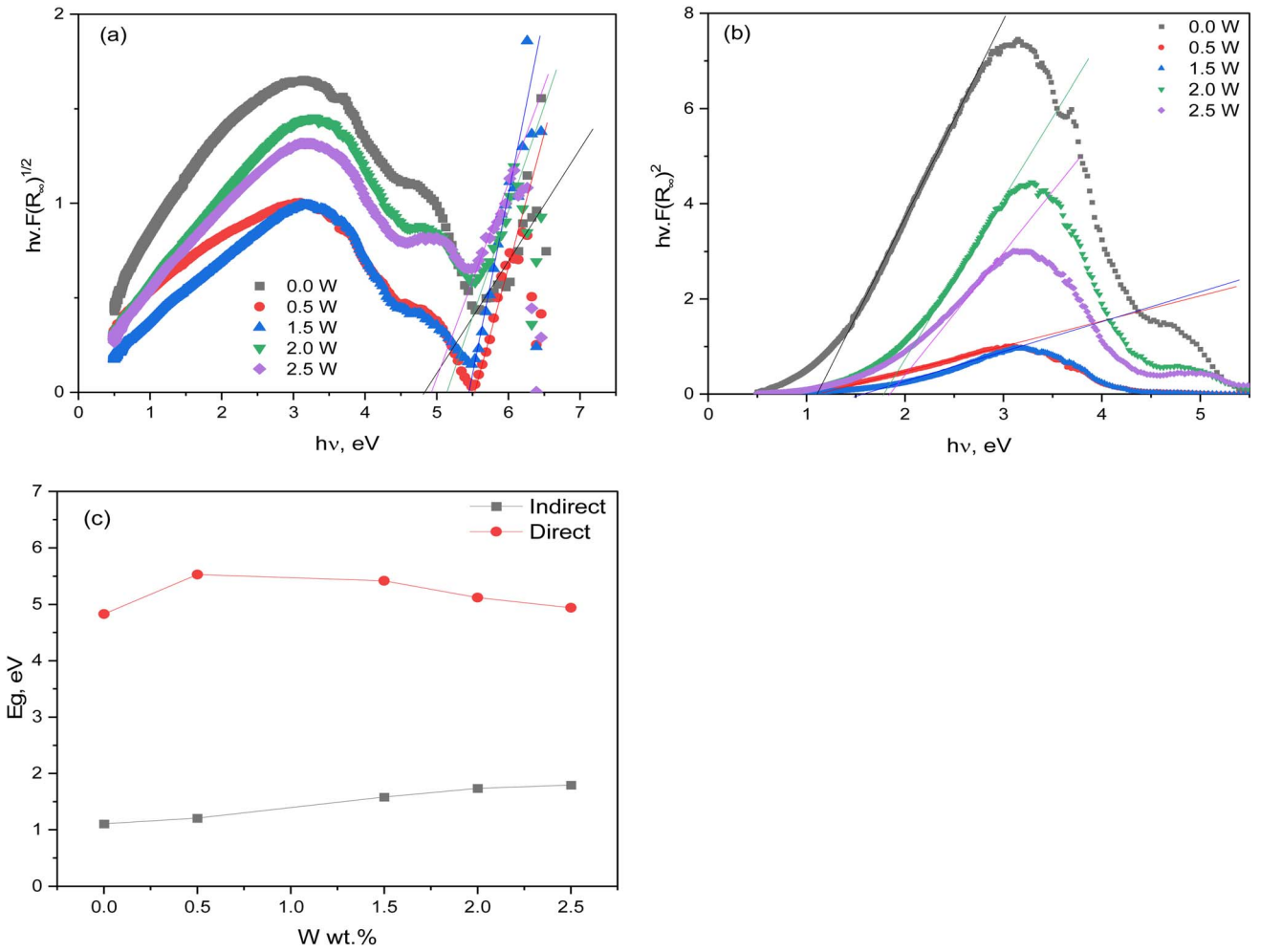

Fig. 11 The Kubelka–Munk function *versus* incident photon energy for (a) direct and (b) indirect cases. (c) the dependence of band gap on tungsten addition.

attempts,[110] such as the Moss relation, Ravindra relation, Herve–Vandamme relation, Reddy relation, Kumar and Singh relation, and Anani relation, have been explored to establish a precise connection between these two parameters. A newly proposed relation[111] successfully accommodates experimental data, spanning both low and high energy ranges. This achievement surpasses comparisons with earlier relations:

$$n = \sqrt{\frac{A}{E_g^{0.5}} - B} \text{ where } A = 3.44^2 \text{ and } B = 3.44^{0.5} \quad (9)$$

The refractive indices of the present nanocomposites were computed using the recent model for an indirect transition case, as illustrated in Fig. 10a. The refractive index's variation in response to W content reverses the band gap's behavior as stated by the model.[110,111] The small change in refractive index establishes these samples as well-suited for armed, astronomical, or visual applications.[110]

The dielectric constant ($\varepsilon_\infty = n^2$),[110] a critical parameter linked to electrical charge storage, is graphically represented in Fig. 12a for the prepared samples in the indirect gap case. Notably, the observed change in the dielectric constant closely aligns with the variation in the refractive index with W content, as indicated by the relation.

Understanding chemical bonding and expecting physical parameters relies heavily on optical electronegativity ($\Delta\chi$). Duffy[112] and Reddy[113] delved into the intricate association of band gap and optical electronegativity as $\Delta\chi^* = 0.2688\ E_g$ (eV) and $\Delta\chi^* = 9.8\ e^{-n}$ (eV), respectively. The optical electronegativity of the current samples in an indirect transition event was meticulously calculated using the two relations presented in Fig. 12b. Notably, the figure unveils a subtle increase in optical electronegativity with the W content. Following Pauling's[114] insights, high $\Delta\chi^*$ signifies ionic character, while lower values indicate covalency. The variations in the optical properties as the W content changes are attributed to the size and distribution of W-containing particles. These particles introduce extra free carriers and interactions among carriers, which lead to the creation of defect states related to W.[97,115,116] These states contribute to the band tailing. They introduce additional free carriers, and carrier interactions induce the formation of W-related defect states that contribute to band tailing. The agreement with XRD analyses confirms the covalent nature of the current samples.

3.7. Electrochemical properties

The CdO-ZnO-W-P_2O_5 (CZWP) with 0%, 0.5%, 1.5%, 2% and 2.5% of tungstate materials have been tested using cyclic voltammetry (CV), linear sweep voltammetry (LSV), galvanostatic charge and discharge (GCD) and electrochemical impedance spectroscopy (EIS) techniques in a mixture of 5 mM ferro/ferri cyanide and 0.1 M KCl as supporting electrolyte. The cyclic voltammogram of the new synthesized nanomaterials was illustrated in Fig. 13A. The fast and high faradaic current was obtained for all modified electrodes with the synthesized CdO-ZnO-W-P_2O_5 (CZWP), while an increasing of the tungsten percentage (0.0% W, 0.5% W, 1.5% W, 2.0% W, and 2.5% W). 0.0% W/modified SPE has the lower faradaic current (anodic peak current: $I_a = 65.2$ and cathodic peak current: $I_c = -92.3$) at 0.21 V and 0.078 V. In 0.5% W/modified SPE the current increased ($I_a = 123.6$ and $I_c = -149.6$) at 0.25 V and 0.083 V. The current of oxidation/reduction peaks increased ($I_a = 203.5$ and $I_c = -181.3$) for 1.5% W/modified SPE at 0.32 V and −0.016 V. The highest faradaic current obtained for 2.0% W modified SPE at 0.2 V and 0.08 V ($I_a = 243.6$ and $I_c = -240.9$) then decreased for 2.5% W/modified SPE ($I_a = 86.2$ and $I_c = -62.1$) at 0.194 V and 0.068 V. The increasing mol% of the tungsten (W) in synthesized CdO-ZnO-W-P_2O_5 (CZWP) nanoparticle structures from 0.0% W up to 2.0% W caused an increase in the faradaic current of the nanoporous due to the conductivity properties of tungsten. The 2.5% W decrease in faradaic current may be due to the steric hindrance effect on the electrode surface. The quantitative electrochemical analysis (I_a, I_c, E_{oxd}, E_{red}, $E_{1/2}$, R_{ct}, C

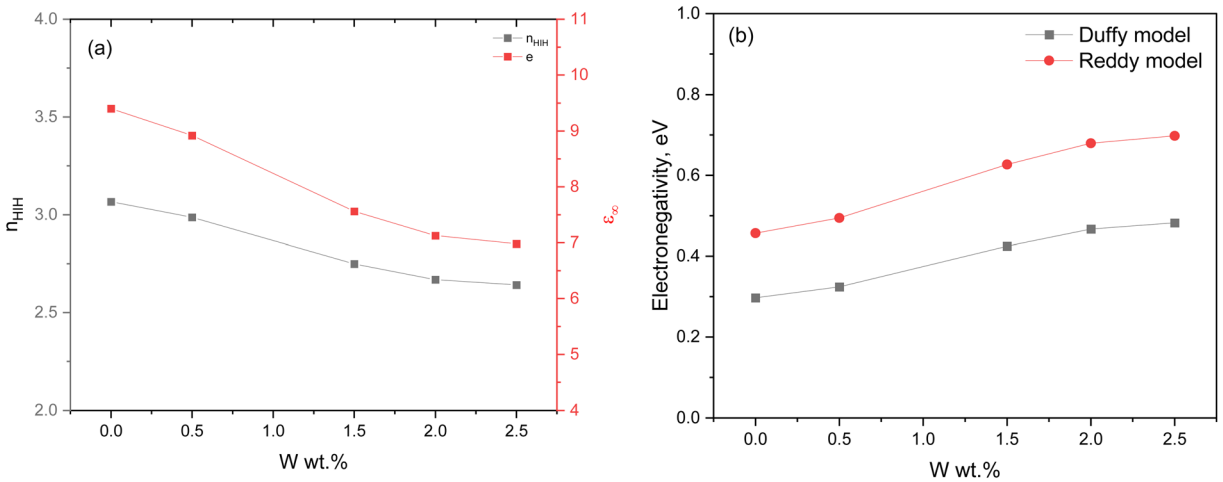

Fig. 12 (a) The refractive index (n) and the dielectric constant in the case of an indirect transition gap, and (b) the calculated optical electronegativity of nanocomposites doped by different W content.

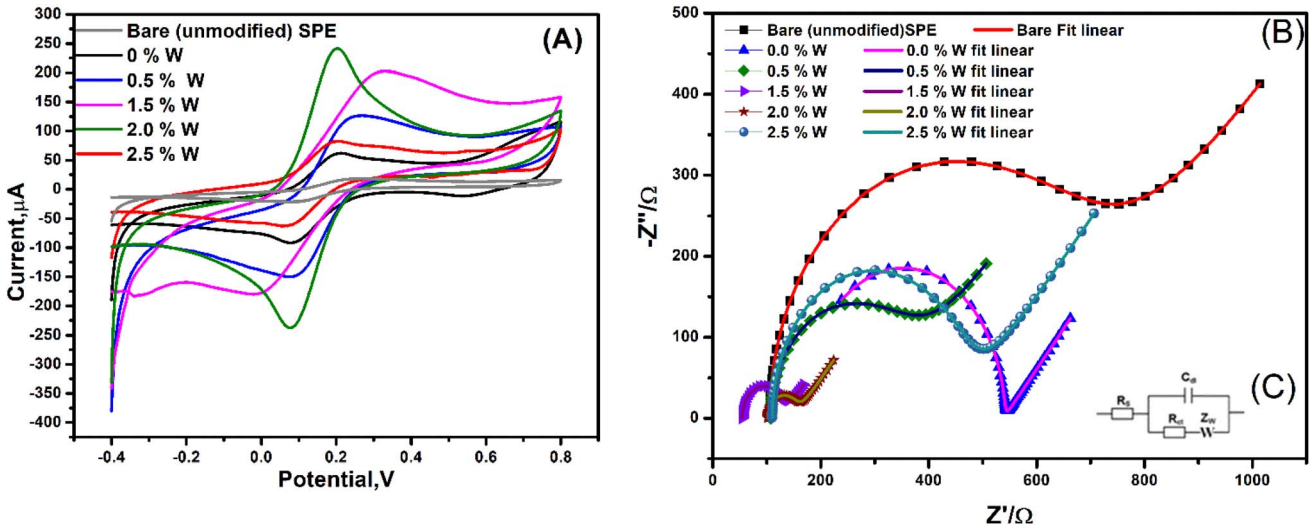

Fig. 13 The (A) CV and (B) EIS measurements of (0, 0.5, 1.5, 2 and 2.5 W) SPEs were measured by using standard redox solution (ferro/ferri cyanide/KCl) with 50 mV s^{-1} scan rate. (C) Circuit which used to fit the Nyquist plot of EIS data.

Table 2 CV and EIS data produced from the experimental work in Fig. 8 for the synthesized materials modified SPEs[a]

Electrode type	I_a (μA)	I_c (μA)	$E_{oxd.}$ (V)	$E_{red.}$ (V)	$E_{1/2}$ (V)	R_s (Ω)	$R_{ct\ (1)}$ (Ω)	CPE	n μF	W (Ω)	Cs (F g^{-1})
Bare (unmodified SPE)	19.1	−21.5	0.22	0.093	0.165	102.3	1150	10.5	0.89	178	—
0% W	65.2	−92.3	0.21	0.078	0.144	101.2	450	15.3	0.85	120.3	1114.2
0.5% W	123.6	−149.6	0.25	0.083	0.16	100.1	352.3	16.5	0.78	117.2	1592.8
1.5% W	203.5	−181.3	0.32	−0.016	0.152	50.3	120.6	17.3	0.84	111.6	2178.5
2% W	243.6	−240.9	0.20	0.08	0.14	99.8	90.2	19.8	0.87	95.8	1764.2
2.5% W	86.2	−62.1	0.194	0.068	0.13	100.3	420	15.9	0.89	118.4	828.5

[a] I_a: anodic current, I_c: cathodic current, E_{oxd}: potential of oxidation E_{red}: potential of reduction, R_s: solution resistance, R_{ct}: charge transfer resistance, CPE: constant phase element, W: Warburg resistance, C is specific capacitance of the electrodes at scan rate of 50 mV s^{-1}.

and W) 0% W, 0.5% W, 1.5% W, 2% W, and 2.5% W modified SPEs are presented in Table 2.

From the Nyquist plots (see Fig. 13B) we can see at high frequency a semicircle, which represents the electron transfer and the semicircle diameter represented the electrode interface charge transfer resistance (R_{ct}). However, the charge transfer resistance of 0.0% W/SPE ($R_{ct} = 450$ Ω), 0.5% W/SPE ($R_{ct} = 352.3$ Ω) and 1.5% W/SPE ($R_{ct} = 120.6$ Ω). The smaller semicircle diameter becomes at 2 W/SPE (90.2 Ω) (see Table 2), referring to a higher efficiency for electron transfer then R_{ct} value ($R_{ct} = 420$ Ω) increases for 2.5% W/SPE. Therefore, the 2.0% W synthesized nanomaterials have a good conductivity and are interesting for a different electrochemical application.

To explore more about the electrochemically active surface area of the modified SPEs with the synthesized CdO-ZnO-W-P_2O_5 (CZWP) nanoporous materials, with 0.0%, 0.5%, 1.5%, 2.0% and 2.5% of tungstate and unmodified SPE voltammetric experiments were consequently performed at different scan rates in the ferricyanide (FCN) solution. As shown in Fig. 14A–F, all used electrodes demonstrated a linear increase in the redox current while the applied scan rates were increasing. However, the highest generated linear redox reactions against the increase in the scan rate was produced by the CdO-ZnO-W-P_2O_5 (CZWP) nanoporous materials, with 2.0%, as shown in Fig. 14E. Relying on the Randles–Sevcik equation:[36]

$$I_p = 2.69 \times 10^5 \times n^{3/2} \times A \times D^{1/2} \times Cu^{1/2} \quad (10)$$

where the I_p, n, D, A, C, and u are standing for the oxidation peak current (in amperes), the number of transferred electrons, diffusion coefficient (cm^2 s^{-1}), electrochemically active surface area (cm^2), concentration of the FCN (molarity), and the scan rate (V s^{-1}), respectively.

The anodic peak current (I_{pa}) and cathodic peak currents (I_{pc}) of the FCN redox reactions were plotted against the square root of the scan rate, as shown inset Fig. 14A–F. To that end, a good linearity with a correlation coefficient of 0.9966. Consequently, the effective electrochemically active surface area of unmodified *vs.* the modified electrode surfaces with 0.0% W, 0.5% W, 1.5% W, 2% W and 2.5% W were calculated. Accordingly, a significant enlargement in the active surface area of the modified electrodes was achieved, the active surface area of the SPE unmodified was 0.567 cm^2, while the surface area of modified electrodes with 2.0% W was 17.2 cm^2. Interestingly,

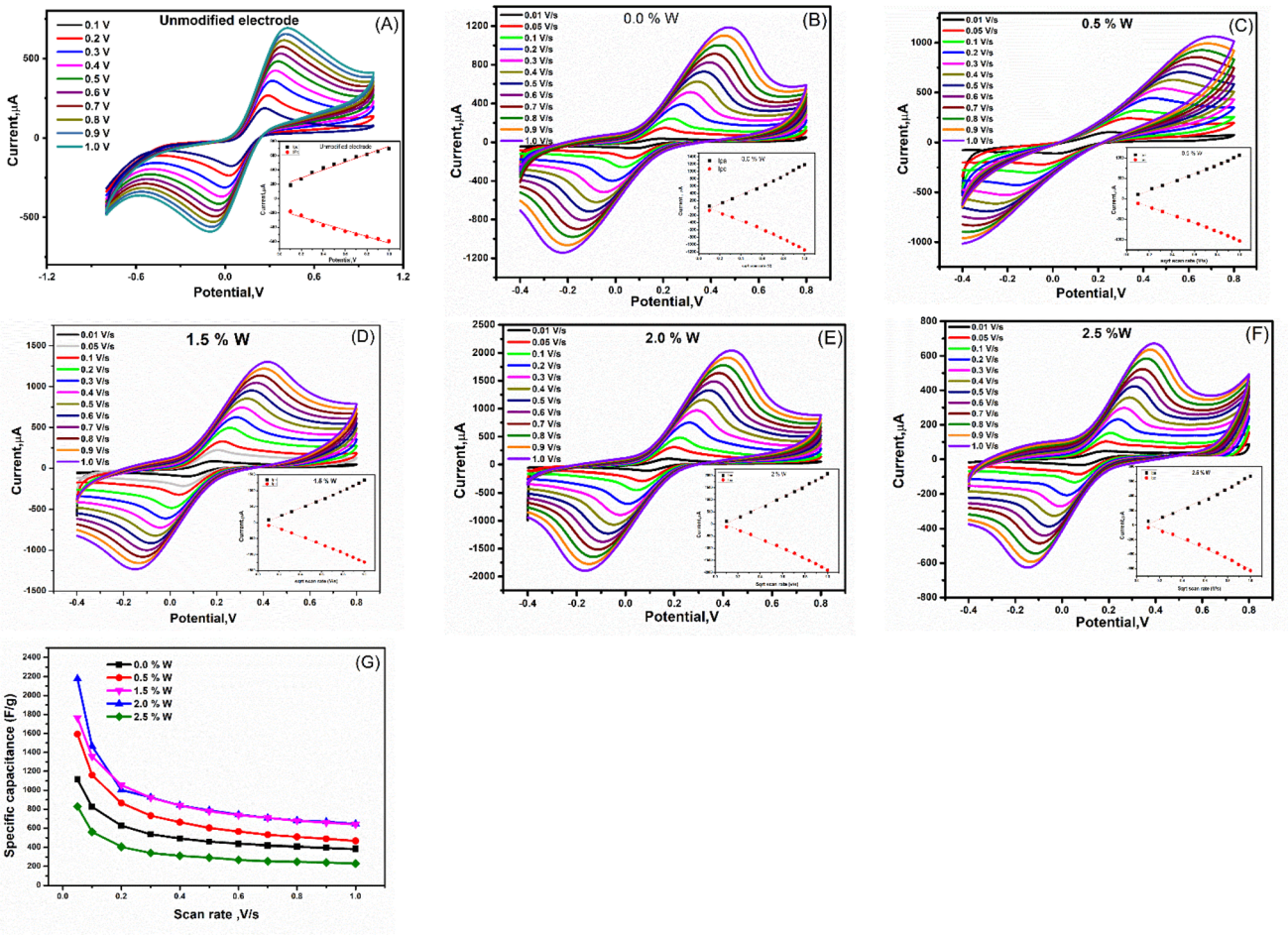

Fig. 14 (A–F) CVs for synthesized CdO-ZnO-W-P_2O_5 (CZWP) with different % of tungsten (W) modified SPEs at different scan rates and the inset figures are I_{pa} and I_{pc} curves of all modified SPEs at different scan rates. (G) Specific capacitance of CZWP with 0.0% W, 0.5% W, 1.5% W, 2.0% W and 2.5% W modified SPE at different scan rates.

the SPE modified with the CdO-ZnO-W-P_2O_5 (CZWP) nanoporous materials, with 2.0% W, exhibited the highest expansion in the electrode active surface area (*i.e.* almost 17-fold increase in order or magnitude).

Furthermore, the specific capacitance was calculated from the following equation:

$$C = \frac{\int I\mathrm{d}V}{2 \times \nu \times m \times \Delta V} \quad (11)$$

where C (F g^{-1}) represent the specific capacitance, IdV is the area under voltammetric peaks, ΔV (V) is the potential window, m (g) is the mass of the active material and ν (V s^{-1}): is the scan rate.

It is worth mentioning here that all materials were electrochemically stable over different applied scan rates, and no damage occurred in the electrode composition.

The large enhancements are obtained in the electrochemical performance after the electrode surfaces were modified with the synthesized CdO-ZnO-W-P_2O_5 (CZWP) with different wt% of the tungsten (0 W, 0.5 W, 1.5 W, 2 W, and 2.5 W) compared with the bare (unmodified) electrode. The CdO-ZnO-W-P_2O_5 (CZWP) with 2.0% of tungstate (W) composite displayed higher specific capacitance (C_s) than that of CdO-ZnO-W-P_2O_5 (CZWP) with 0.0%, 0.5%, 1.5% and 2.5% of W (see Fig. 14G and Table 2) at all tested scan rates. The obtained specific capacitance for the CZWP with 2.0% W (2178 F g^{-1} at 50 mV s^{-1}) is much higher than that cited for CZWP with 0.0% W (1114.2 F g^{-1} at 50 mV s^{-1}), 0.5% W (1592.8 F g^{-1} at 50 mV s^{-1}), 1.5% W (1764 F g^{-1} at 50 mV s^{-1}) and 2.5% W (828 F g^{-1} at 50 mV s^{-1}).

Therefore, the perfect composite contains 2.0% W. The results show that the ratio of W has a noteworthy impact on the electrochemical performance of the modified electrodes. Initially, an increase in W content improves the faradaic current, success its peak at 2.0% W. This proposes that 2% W is the optimal ratio for maximum electrochemical activity. However, increasing the W percentage content beyond this point results in a decrease in current. This may be due to the over-saturation or clumping together of W nanoparticles, which can hinder electron transfer developments.[117,118] This pattern emphasizes the standing of fine-tuning the W content to realize the best electrochemical performance in CdO-ZnO-W-P_2O_5 nanoporous structures. The strong enhancement is owing to the enlarged surface area of the SPE surface after modification of the synthesized synthesized CdO-ZnO-W-P_2O_5 (CZWP), which

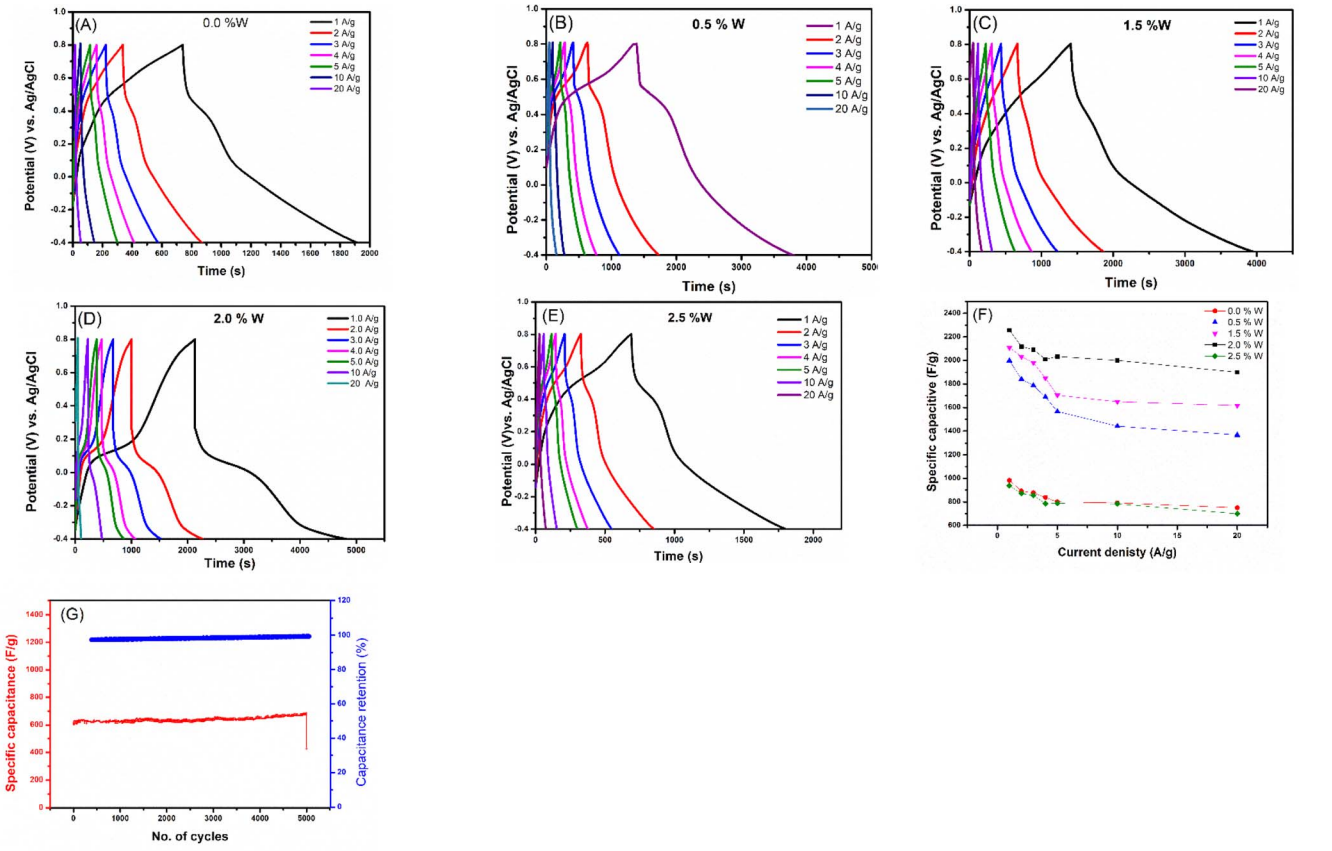

Fig. 15 3-electrode cell electrochemical performance for the fabricated CdO-ZnO-W-P_2O_5 (CZWP) with different wt% of the tungsten (0.0% W, 0.5% W, 1.5% W, 2.0% W, and 2.5% W) electrodes in 5 mM ferro/ferri cyanide/0.1 M KCl electrolyte. (A–E): GCD profiles at various applied current densities (1.0–20 A g^{-1}), (F): specific capacitance *versus* applied current densities. (G): cyclability test over 5000 GCD cycles.

produces an increase in the surface conductivity and its electrocatalytic activity. Consequently, the new synthesized CdO-ZnO-W-P_2O_5 (CZWP) composites are very promising in different electrochemical applications such as biosensors, sensors, and energy storage.

The linear sweep voltammetry (LSV) curves of the synthesized CdO-ZnO-W-P_2O_5 (CZWP) with different % of tungsten (W) modified SPEs at different scan rate are illustrated in Fig. S1(A–E).† The LSV curves show agreement with CVs curves for oxidation peaks in the potential range between −0.4 to +0.8 V.

The galvanostatic charge/discharge (GCD) characteristics are required to clarify the validity of the synthesized CdO-ZnO-W-P_2O_5 (CZWP) with different wt% of the tungsten (0.0% W, 0.5% W, 1.5% W, 2.0% W, and 2.5% W) for use to construct supercapacitor devices. The C_s at different current densities was calculated from the GCD graphs through eqn (12):

$$C_s = I\Delta t/m\Delta V \quad (12)$$

where I is the discharged current (A), ΔV is the potential window (V), and Δt is the discharged time (s), m is the mass of the deposited electrode material (g).

Table 3 Comparison of the produced C_s with those reported in literature for phosphate-based electrodes

Material	Electrolyte	Specific capacitance (current density)	Ref.
Nickel–zinc phosphate microspheres with carbon dots	3.0 M KOH	1885.7 F g^{-1} (1 A g^{-1})	120
$Ni_3(PO_4)_2$/RGO/$Co_3(PO_4)_2$	1 M KOH	1137.5 F g^{-1} (0.5 A g^{-1})	121
Porous $Ni_2P/Co_2(P_2O_7)$	3 M KOH	1720 F g^{-1} (1.0 A g^{-1})	122
$Ni_3(PO_4)$ in Ag_3PO_4	1 M KOH	539 F g^{-1} (1 A g^{-1})	123
Cobalt pyrophosphate	3.0 M KOH	367.2 F g^{-1} (0.625 A g^{-1})	124
Tungsten-doped cadmium zinc phosphate nanoporous	5 mM potassium ferro/ferricyanide +0.1 M KCl	2257 F g^{-1} (1 A g^{-1})	This work

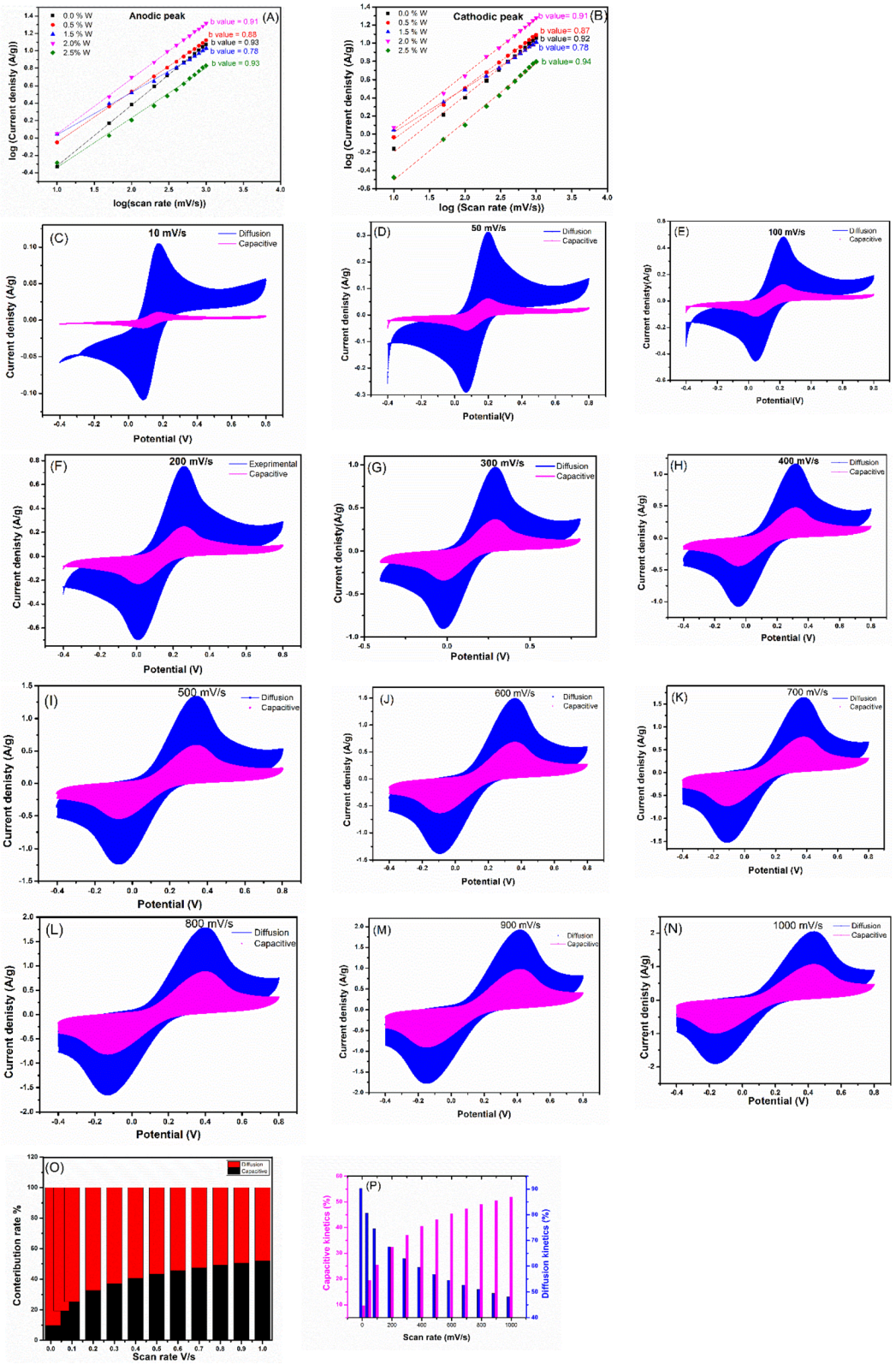

Fig. 16 (A) *b*-value measured *versus* Ag/AgCl during the anodic scan and (B) during the cathodic scan. (C–N) Deconvoluted voltammograms into capacitive (purple) and diffusive (blue) at different scan rates 10, 50, 100, 200, 300, 400, 500, 600, 700, 800, 900 and 1000 mV s^{-1}. (O) Capacitance values divided into capacitive and diffusive components at various scan rates (10–10000 mV s^{-1}). (P) Contributions percentages of diffusive and capacitive kinetics at different scan rates (10–1000 mV s^{-1}).

The GCD capacitance at 1 A g^{-1} of the CdO-ZnO-W-P_2O_5 (CZWP) with 2.0% W composite (2257 F g^{-1}) is higher than that of the CdO-ZnO-W-P_2O_5 (CZWP) with 1.5% W (2108 F g^{-1}), 0.5% W (1998 F g^{-1}), 0.0% W (982 F g^{-1}) and 2.5% W (937 F g^{-1}), The obtained GCD graphs at various current densities (1, 2, 3, 4, 5, 10 and 20 A g^{-1}) for the fabricated CdO-ZnO-W-P_2O_5 (CZWP) with different wt% of the tungsten (0.0% W, 0.5% W, 1.5% W, 2.0% W, and 2.5% W) electrodes are depicted in Fig. 15A–E. All the GCD curves, revealing the high electrical conductivity of the synthesized materials that ensures fast and capable transfer of charges,[119] owing to the highly conductivity of tungsten. The change of the C_s with current density (see Fig. 15F), revealing an inverse relationship. The C_s values obtained from the GCD graphs of the nanoporous CZWP with 2.0% W were 2257, 2118, 2092, 2010, 2033, 2000 and1900 F g^{-1} at 1.0, 2.0, 3.0, 4.0, 5.0, 10.0 and 20.0 A g^{-1}, respectively. Note that the achieved C_s at 1.0 A g^{-1} (2257 F g^{-1}) is almost similar to that computed from the CVs (2178.5 F g^{-1}) at 50 mV s^{-1}. The C_s of CZWP with 1.5% W are 2108, 2033, 1982, 1850, 1704, 1650, 1616 F g^{-1} at 1.0, 2.0, 3.0, 4.0, 5.0, 10.0 and 20.0 A g^{-1}, respectively. For CZWP with 0.5% W, the C_s values are 1998, 1841, 1787, 1690, 1566, 1441 F g^{-1} at 1.0, 2.0, 3.0, 4.0, 5.0, 10.0 and 20.0 A g^{-1}, respectively and for CZWP with 0.5% W the C_s obtained values are 1998, 1841, 1787, 1690, 1566 F g^{-1} at 1.0, 2.0, 3.0, 4.0, 5.0, 10.0 and 20.0 A g^{-1}. For CZWP with 2.5% W the specific capacitances (C_s) are 937, 871, 855, 786, 785, 783, 700 F g^{-1} at 1.0, 2.0, 3.0, 4.0, 5.0, 10.0 and 20.0 A g^{-1}.

The GCD capacitance at 1 A g^{-1} of the CdO-ZnO-W-P_2O_5 (CZWP) with 2.0% W composite (2257 F g^{-1}) is higher than that of 1.5% W (2108 F g^{-1}), 0.5% W (1998 F g^{-1}), 0.0% W (982 F g^{-1}) and 2.5% W (937 F g^{-1}), the C_s of the composite CZWP with 2.0% W is higher than those cited for phosphate-based electrodes in the literature,[120–124] see Table 3.

The cycling stability life test of the composite CZWP with 2.0% W has been elucidated *via* the GCD tests at 3 A g^{-1} for 5000 cycles (see Fig. 15G). The modified electrode maintained 98.8% capacitance after 5000 cycles and 96.6% after 5000 cycles, revealing the outstanding cycling stability of the composite CZWP with 2.0% W.

The electrochemical kinetics were studied to understand the charge storage process of synthesized CdO-ZnO-W-P_2O_5 (CZWP) with different wt% of the tungsten (0.0% W, 0.5% W, 1.5% W, 2% W, and 2.5% W) by using Power-law, eqn (13).[125]

$$\log(i) = b\log(v) + \log(a) \tag{13}$$

where v is the scan rate, i is the peak current density, and a and b are arbitrary constants. The b-value is determined at each potential (V) by plotting log i *vs.* log(v) and evaluating the linear-fitted graph slope. Fig. 16A and B shows the linear-fitted plots together with calculated b-values at a applied potentials, namely 0.42, 0.40, 0.65, 0.44, 0.38 V *versus* Ag/AgCl, during the anodic (from −0.40 V to +0.8 V) and −0.22, −0.152, −0.37, −0.167, and 0.16 V during cathodic scan (from +0.8 V to −0.4 V) for CZWP with 0.0, 0.5, 1.5, 2.0 and 2.5% W respectively. The derived b-values for the CZWP with 0.0, 0.5, 1.5, 2.0 and 2.5% W modified electrodes during the anodic scan (0.93, 0.88, 0.78, 0.91, 0.93) and cathodic scan (0.92, 0.87, 0.78, 0.91, 0.94) suggesting that capacitive and diffusion processes are involved in the overall storage.

The quantitative current contribution *via* surface-capacitive and diffusive-faradaic mechanisms can be evaluated from the total current following Dunn's method. In this method, the total voltammetric current $i(V)$ is the sum of capacitive and diffusive contributions as follows:[126,127]

$$i(V) = av^b = i_{cap} + i_{diff} \tag{14}$$

or,

$$i(V)/v_{0.5} = xv_{0.5} + y \tag{15}$$

The x and y constants are obtained from the slope and intercept of the relationship between $i(V)/v_{0.5}$ *versus* $v_{0.5}$ curve. Using x and y values at each potential V, the current contribution for capacitive (xv) and diffusive ($yv_{0.5}$) kinetics can be measured. The results of capacitive and diffusive regions are presented in Fig. 16C–N at a scan rate of 10, 50, 100, 200, 300, 400, 500, 800, 900 and 1000 mV s^{-1}.

Table 4 and Fig. 16O and P presents the calculated contribution percentages of diffusion-controlled faradaic and surface-controlled capacitive processes at scan rates from 10 to 1000 mV s^{-1}.

Conspicuously, the capacitive kinetics contributes (51.82%) higher than diffusive kinetics (48.18%) at 1000 mV s^{-1}. In contrast, at the lowest scan rate (10 mV s^{-1}), the diffusive kinetics (90.28%) contribution percentage was higher than the capacitive (9.71%) kinetics. However, at 500 mV s^{-1}, the contribution percentage of diffusive kinetics (56.79%) overtakes the capacitive kinetics (43.20%). Thus, with increasing in the scan rate from 10 to 1000 mV s^{-1}, the capacitive contribution keeps increasing while the diffusive contribution decreasing. In total, the faster capacitive or pseudocapacitive kinetics largely dominate the overall current for the CZWP with 2.0% W electrode at higher scan rates, while the diffusive kinetics are limited owing to the inadequacy of slower diffusion-limited faradaic kinetics at higher rates.

Table 4 The calculated contribution percentages of diffusion and capacitive at scan rates from 10 to 1000 mV s^{-1}

Scan rate mV s^{-1}	I capacitive contribution %	I diffusion contribution %
10	9.71284	90.28716
50	19.39058	80.60942
100	25.38365	74.61635
200	32.4826	67.5174
300	37.07623	62.92377
400	40.48957	59.51043
500	43.20394	56.79606
600	45.45323	54.54677
700	47.36995	52.63005
800	49.03678	50.96322
900	50.50893	49.49107
1000	51.82515	48.17485

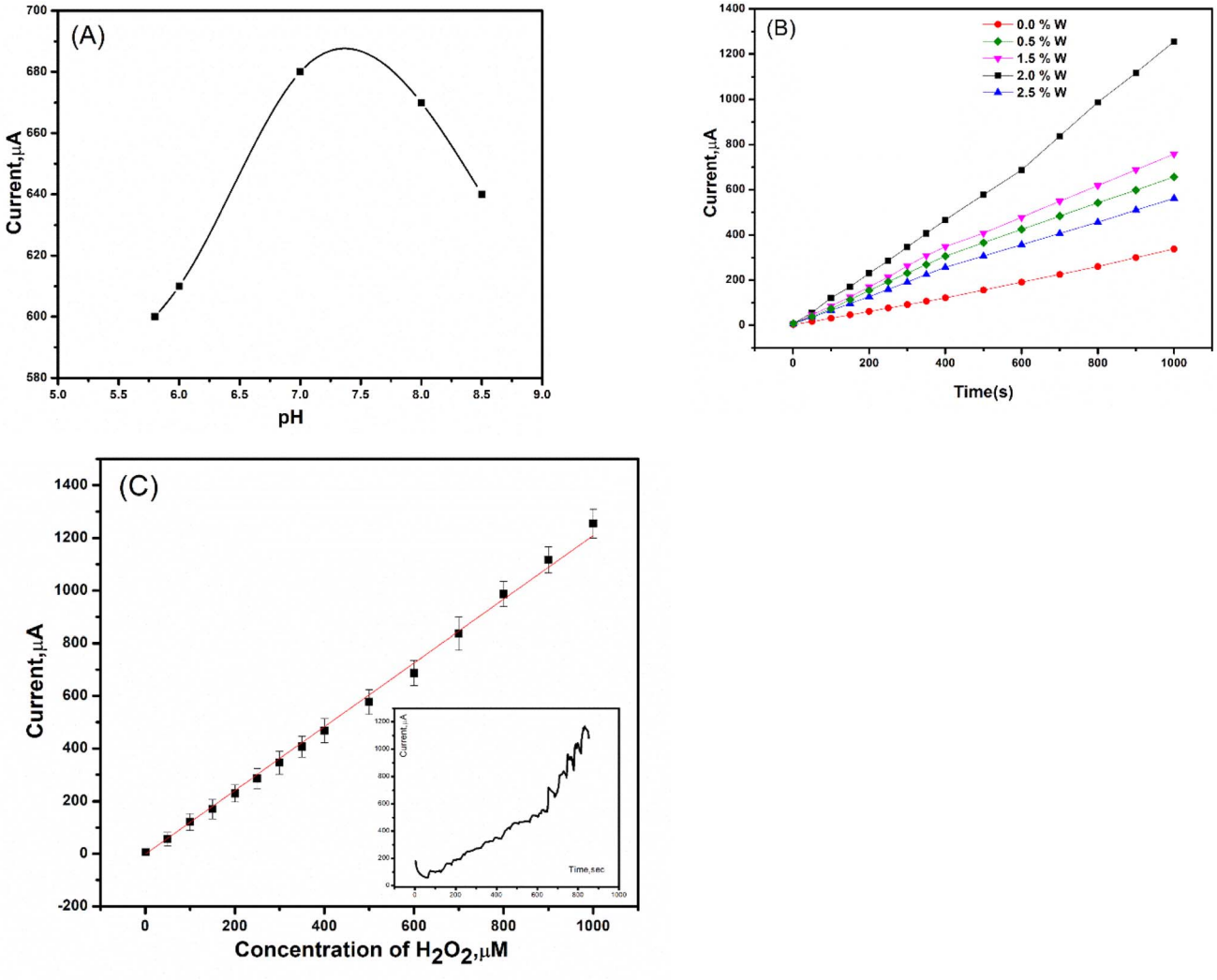

Fig. 17 (A) The pH effect study on 2 W/SPE performance towards the peroxide sensitivity. (B) The corresponding calibration curve of 0 W, 0.5 W, 1.5 W, 2 W and 2.5 W modified SPE toward H_2O_2 response. (C). The corresponding calibration curve of 2 W modified SPE toward H_2O_2 response.

3.8. The use of synthesized nanoporous materials for H_2O_2 detection

Due to the high electrocatalytic activity of the CZWP with 2.0% W, which is approved by CV study, it promotes fast electron transfer and direct oxidation in biosensor applications. Thus, the testing of direct electron transfer, which is produced from the oxidation of peroxide, was studied for CZWP with 2.0% W/modified SPE.

3.8.1 pH effect study. The pH of buffer-supporting electrolytes was affected by the electrochemical properties of the biosensor. Therefore, different pHs of the phosphate buffer toward the oxidation of peroxide were tested using 2 W/SPE and chronoamperometric technique (Fig. 17A). The pH value increased from 5.75 up to 7.0 then decreased. So, the phosphate buffer with a pH = 7.0 will be used for all of the following experiments.

3.8.2 Amperometric method for peroxide detection. The amperometric detection of peroxide for 0 W, 0.5 W, 1.5 W, 2 W, and 2.5 W modified SPEs was produced by adding a certain amount of peroxide at a fixed time (50 seconds). The relation between the peroxide concentrations and the response of current (Fig. 17B) showed a fast and high response for all modified SPEs, which approved the fast electron transfer. Furthermore, the fast and highest response toward peroxide oxidation produced by using 2 W/SPE (Fig. 17C) with a wide linear range from 1.0–1000 μM and detection limit of 0.025 μM (S/N = 5) compared with the literature[31,38,128–130] Therefore it is effective to use modifier's materials for the enzymatic-based biosensors application.

4 Conclusion

This study successfully synthesized and characterized CZWP nanostructures doped with tungsten through a sol–gel process, demonstrating their multifunctional potential in energy storage and sensing applications. Tungsten doping significantly influenced the structural, optical, and electrochemical properties of the material. The XPS survey confirms the successful formation

of CZPO NPs and doped 2.5 W. The shifts in Zn, Cd, and O binding energies, with adding W support the chemical states and electronic structure changes induced by doping in phosphate-based nanomaterials. The BET analysis demonstrates that tungsten doping significantly enhances the surface area and porosity of CdZnPs, improving their utility for catalytic and energy-related applications. The material's mesoporous nature makes it a promising candidate for efficient mass transport and controlled surface interactions in advanced technologies. Notably, the 2% W-doped samples exhibited optimal performance, with enhanced specific capacitance, efficient electron transfer, and exceptional H_2O_2 sensing capabilities. The integration of these nanostructures into supercapacitor electrodes and biosensor platforms offers a sustainable and efficient approach to addressing the increasing energy demands and advancing sensing technologies. These results provide a robust foundation for further exploration and development of CZWP-based nanomaterials in cutting-edge applications.

Data availability

All data generated or analyzed during this study are included in this published article and will be available upon request to the author.

Author contributions

All authors conceived and designed the experiments; analyzed and interpreted the data; contributed reagents, materials, analysis tools, or data; and wrote the paper.

Conflicts of interest

The authors declare no competing interests.

Acknowledgements

The work was supported by grant numbers 13020232 and 13020103. The National Research Centre of Egypt facilitates the work and the characterization tools.

References

1 A. B. A. Hammad, H. S. Magar, A. M. Mansour, R. Y. A. Hassan and A. M. E. Nahrawy, Construction and characterization of nano-oval BaTi0.7Fe0.3O3@NiFe2O4 nanocomposites as an effective platform for the determination of H2O2, *Sci. Rep.*, 2023, 13.

2 B. Wang, L. Luo, X. Jiang, W. Li and H. Chen, Energy-storage properties of (1−x)Bi0.47Na0.47Ba0.06TiO3–xKNbO3 lead-free ceramics, *J. Alloys Compd.*, 2014, **585**, 14–18.

3 A. B. Abou Hammad, A. M. Mansour and A. M. El Nahrawy, Ni2+ doping effect on potassium barium titanate nanoparticles: enhancement optical and dielectric properties, *Phys. Scr.*, 2021, **96**, 125821.

4 S. M. Al-Hindawey, A. M. El Nahrawy, A. I. Ali and H. A. Zayed, Magnetic states in Fe-doped Bi2Se3 topological insulators nano-crystallites, *Int. J. Mater. Eng. Innovation*, 2021, **12**, 325–336.

5 S. Ranganatha, A short review on metal phosphide based 2D nanomaterials for high performance electrochemical supercapacitors, *Mater. Res. Innovations*, 2023, **27**, 93–99.

6 M. Ates, A. Chebil, O. Yoruk, C. Dridi and M. Turkyilmaz, Reliability of electrode materials for supercapacitors and batteries in energy storage applications: a review, *Ionics*, 2022, **28**, 27–52.

7 R. Ahmed and G. Nabi, Morphology tailoring and enhanced electrochemical properties of Cd–Zn co-doped NiO nanorods for high performance supercapacitor, *Ceram. Int.*, 2020, **46**, 22330–22337.

8 D. T. Dam, X. Wang and J.-M. Lee, Graphene/NiO Nanowires: Controllable One-Pot Synthesis and Enhanced Pseudocapacitive Behavior, *ACS Appl. Mater. Interfaces*, 2014, **6**, 8246–8256.

9 B. Dunn, H. Kamath and J.-M. Tarascon, Electrical Energy Storage for the Grid: A Battery of Choices, *Science*, 2011, **334**, 928–935.

10 M. I. Pratheepa and M. Lawrence, Eco-friendly approach in supercapacitor application: CuZnCdO nanosphere decorated in reduced graphene oxide nanosheets, *SN Appl. Sci.*, 2020, **2**, 318.

11 A. M. El Nahrawy, A. B. A. Hammad, A. M. Bakr, B. A. Hemdan and A. R. Wassel, Decontamination of ubiquitous harmful microbial lineages in water using an innovative Zn2Ti0.8Fe0.2O4 nanostructure: dielectric and terahertz properties, *Heliyon*, 2019, **5**, e02501.

12 A. M. El Nahrawy, A. S. Montaser, A. M. Bakr, A. B. Abou Hammad and A. M. Mansour, Impact of ZnO on the spectroscopic, mechanical, and UPF properties of Fe2O3-tough polystyrene-based nanocomposites, *J. Mater. Sci.: Mater. Electron.*, 2021, **32**, 28019–28031.

13 A. A. Elabd, O. A. Elhefnawy and A. M. El Nahrawy, A new organic-silica based nanocomposite prepared for spectrophotometric determination of uranyl ions, *RSC Adv.*, 2016, **6**, 9563–9570.

14 D. Bokov, A. Turki Jalil, S. Chupradit, W. Suksatan, M. Javed Ansari, I. H. Shewael, G. H. Valiev and E. Kianfar, Nanomaterial by Sol-Gel Method: Synthesis and Application, *Adv. Mater. Sci. Eng.*, 2021, **2021**, 5102014.

15 A. A. Ansari, M. A. M. Khan and S. Ameen, Ln2O3:Eu nanoparticles: host lattices and their impact on photoluminescence, Raman, optical, and crystal properties, *J. Nanopart. Res.*, 2023, **25**, 1–16.

16 S. Arya, P. Mahajan, S. Mahajan, A. Khosla, R. Datt, V. Gupta, S.-J. Young and S. K. Oruganti, Review—Influence of Processing Parameters to Control Morphology and Optical Properties of Sol-Gel Synthesized ZnO Nanoparticles, *ECS J. Solid State Sci. Technol.*, 2021, **10**, 23002.

17 A. M. Abouelnaga, A. M. Mansour, A. B. Abou Hammad and A. M. El Nahrawy, Optimizing magnetic, dielectric, and antimicrobial performance in chitosan-PEG-Fe2O3@NiO

nanomagnetic composites, *Int. J. Biol. Macromol.*, 2024, **260**, 129545.

18 A. M. El Nahrawy, B. A. Hemdan, A. B. Abou Hammad, A. M. Othman, A. M. Abouelnaga and A. M. Mansour, Modern Template Design and Biological Evaluation of Cephradine-loaded Magnesium Calcium Silicate Nanocomposites as an Inhibitor for Nosocomial Bacteria in Biomedical Applications, *Silicon*, 2021, **13**, 2979–2991.

19 A. M. El Nahrawy, A. Elzwawy, M. M. Alam, B. A. Hemdan, A. M. Asiri, M. R. Karim, A. B. A. Hammad and M. M. Rahman, Synthesis, structural analysis, electrochemical and antimicrobial activities of copper magnesium zirconosilicate (Cu20Mg10Si40Zr(30-x)O:(x = 0,5,7,10) Ni2+) nanocrystals, *Microchem. J.*, 2021, **163**, 105881.

20 M. Catauro, E. Tranquillo, G. Dal Poggetto, M. Pasquali, A. Dell'Era and S. V. Ciprioti, Influence of the heat treatment on the particles size and on the crystalline phase of TiO2 synthesized by the sol-gel method, *Materials*, 2018, **11**(12), 2364.

21 A. Fazal, M. J. Iqbal, M. A. Raza, B. S. Almutairi, M. Z. Iqbal, T. Subhani, S. Riaz and S. Naseem, Binder-free hydrothermal approach to fabricate high-performance zinc phosphate electrode for energy storage applications, *Ceram. Int.*, 2024, **50**, 2742–2753.

22 S. Naghash-Hamed, N. Arsalani and S. B. Mousavi, The catalytic performance of CuFe2O4@CQD nanocomposite as a high-perform heterogeneous nanocatalyst in nitroaniline group reduction, *Sci. Rep.*, 2023, **13**, 3329.

23 A. S. Abouhaswa, G. M. Turky, T. S. Soliman and O. Structural, Dielectric Properties of PVA-CMC/Ni0.65Cu0.35Fe2O4 Films for Optoelectronic Applications and Energy Storage Applications, *J. Inorg. Organomet. Polym. Mater.*, 2023, **34**, 1699–1711.

24 K. Dhamodharan, R. Yuvakkumar, V. Thirumal, G. Ravi, M. Isacfranklin, S. A. Alharbi, T. A. Alahmadi and D. Velauthapillai, Effect of Nd3+ doping on CdO nanoparticles for supercapacitor applications, *Ceram. Int.*, 2021, **47**, 30790–30796.

25 P. Christuraj, M. D. Raja, S. Pari, D. Madankumar and V. U. Shankar, Synthesis and characterization of Zn doped CdS nanoparticles as electrode material for supercapacitor application, *Mater. Today: Proc.*, 2020, **50**, 2691–2694.

26 N. Anwar, A. Shakoor, G. Ali, H. Ahmad, N. A. Niaz, S. Arooj and A. Mahmood, Synthesis and electrochemical characterization of polyaniline doped cadmium oxide (PANI-CdO) nanocomposites for supercapacitor applications, *J. Energy Storage*, 2022, **55**, 105446.

27 M. I. Pratheepa and M. Lawrence, Synthesis of pure, Cu and Zn doped CdO nanoparticles by co-precipitation method for supercapacitor applications, *Vacuum*, 2019, **162**, 208–213.

28 A. A. Ansari, R. Lv, S. Gai, A. K. Parchur, P. R. Solanki, A. Archana, Z. A. Ansari, M. Dhayal, P. Yang, M. K. Nazeeruddin and M. M. Tavakoli, ZnO nanostructures – Future frontiers in photocatalysis, solar cells, sensing, supercapacitor, fingerprint technologies, toxicity, and clinical diagnostics, *Coord. Chem. Rev.*, 2024, **515**, 215942.

29 S. W. Im, H. Ahn, E. S. Park, K. T. Nam and S. Y. Lim, Electrochemically Activated NiFeOxHyfor Enhanced Oxygen Evolution, *ACS Appl. Energy Mater.*, 2021, **4**, 595–601.

30 E. Ouda, N. Yousf, H. S. Magar, R. Y. A. Hassan and E. S. M. Duraia, Electrochemical properties of MnO2-based carbon nanomaterials for energy storage and electrochemical sensing, *J. Mater. Sci.: Mater. Electron.*, 2023, **34**, 1–14.

31 C. C. Kee, K. Ng, B. C. Ang and H. S. C. Metselaar, Synthesis, characterization and in-vitro biocompatibility of electrophoretic deposited europium-doped calcium silicate on titanium substrate, *J. Eur. Ceram. Soc.*, 2023, **43**, 1189–1204.

32 M. Abbas and H. Amer, A Novel Solid-Contact Sensor for Flow Injection Determination of Verapamil in Pharmaceutical Formulations and Urine, *Curr. Pharm. Anal.*, 2008, **4**, 90–100.

33 M. N. Abbas and H. S. Amer, A Solid-Contact Indium(III) Sensor based on a Thiosulfinate Ionophore Derived from Omeprazole, *Bull. Korean Chem. Soc.*, 2013, **34**, 1153–1159.

34 M. S. Hashem, H. S. Magar, A. M. Fahim and R. A. Sobh, Antioxidant-rich brilliant polymeric nanocomposites for quick and efficient non-enzymatic hydrogen peroxide sensor, *RSC Adv.*, 2024, **14**, 13142–13156.

35 R. A. Sobh, H. S. Magar, H. A. A. El Salam and H. E. Nasr, Acrylate polymeric nanocomposites embedded with transition metal triazole complexes: synthesis, characterization, and prospective implement as hydrogen peroxide sensors, *J. Nanopart. Res.*, 2024, **26**, 1–16.

36 H. S. Magar, M. S. Hashem and R. A. Sobh, Design of metal oxide nanoparticles-embedded polymeric nanocomposites for hydrogen peroxide chronoamperometric sensor, *Polym. Compos.*, 2024, **45**, 3653–3665.

37 A. M. Fahim, H. S. Magar and N. H. Mahmoud, Synthesis, antimicrobial, antitumor activity, docking simulation, theoretical studies, and electrochemical analysis of novel Cd(II), Co(II), Cu(II), and Fe(III) complexes containing barbituric moiety, *Appl. Organomet. Chem.*, 2023, **37**(4), e7023.

38 H. S. Magar, R. Y. A. Hassan and A. Mulchandani, Electrochemical Impedance Spectroscopy (EIS): Principles, Construction, and Biosensing Applications, *Sensors*, 2021, **21**(19), 6578.

39 H.-A. S. Tohamy and H. S. Magar, A Flexible, Low-Cost, Disposable Non-Enzymatic Electrochemical Sensor Based on MnO2/Cellulose Nanostructure, *ECS J. Solid State Sci. Technol.*, 2022, **11**, 127003.

40 H. S. Magar, M. N. Abbas, M. B. Ali and M. A. Ahmed, Picomolar-sensitive impedimetric sensor for salivary calcium analysis at POC based on SAM of Schiff base–modified gold electrode, *J. Solid State Electrochem.*, 2020, **24**, 723–737.

41 H. S. Magar, M. E. Ghica, M. N. Abbas and C. M. A. Brett, Highly Sensitive Choline Oxidase Enzyme Inhibition Biosensor for Lead Ions Based on Multiwalled Carbon Nanotube Modified Glassy Carbon Electrodes, *Electroanalysis*, 2017, **29**, 1741–1748.
42 H. S. Magar, E. E. A.-E. Magd, R. Y. A. Hassan and A. M. Fahim, Rapid impedimetric detection of cadmium ions using Nanocellulose/ligand/nanocomposite (CNT/Co3O4), *Microchem. J.*, 2022, **182**, 107885.
43 H. S. Magar, M. E. Ghica, M. N. Abbas and C. M. A. Brett, A novel sensitive amperometric choline biosensor based on multiwalled carbon nanotubes and gold nanoparticles, *Talanta*, 2017, **167**, 462–469.
44 A. Elzwawy, A. M. Mansour, H. S. Magar, A. B. A. Hammad, R. Y. A. Hassan and A. M. El Nahrawy, Exploring the structural and electrochemical sensing of wide bandgap calcium phosphate/CuxFe3-xO4 core-shell nanoceramics for H2O2 detection, *Mater. Today Commun.*, 2022, **33**, 104574.
45 M. S. Hashem and H. S. Magar, Creative synthesis of pH-dependent nanoporous pectic acid grafted with acrylamide and acrylic acid copolymer as an ultrasensitive and selective riboflavin electrochemical sensor in real samples, *Int. J. Biol. Macromol.*, 2024, **280**, 136022.
46 H. S. Magar, A. M. El Nahrawy, R. Y. A. Hassan and A. B. Abou Hammad, Nanohexagonal iron barium titanate nanoparticles surface-modified NiFe2O4 composite screen-printed electrode for enzymatic glucose monitoring, *RSC Adv.*, 2024, **14**, 34948–34963.
47 H. S. Magar, A. M. Fahim and M. S. Hashem, Accurate, affordable, and easy electrochemical detection of ascorbic acid in fresh fruit juices and pharmaceutical samples using an electroactive gelatin sulfonamide, *RSC Adv.*, 2024, **14**, 39820–39832.
48 H. S. Magar, M. Fayez, F. Febbraio and R. Y. A. Hassan, Esterase-2 mutant-based nanostructured amperometric biosensors for the selective determination of paraoxon (Neurotoxin), *Anal. Biochem.*, 2025, **698**, 115751.
49 H. S. Magar, P. K. Brahman and R. Y. A. Hassan, Disposable impedimetric nano-immunochips for the early and rapid diagnosis of Vitamin-D deficiency, *Biosens. Bioelectron.:X*, 2022, **10**, 100124.
50 H. S. Magar, M. S. Hashem and R. A. Sobh, Design of metal oxide nanoparticles-embedded polymeric nanocomposites for hydrogen peroxide chronoamperometric sensor, *Polym. Compos.*, 2024, **45**, 3653–3665.
51 H. S. Magar, R. Y. A. Hassan and M. N. Abbas, Non-enzymatic disposable electrochemical sensors based on CuO/Co3O4@MWCNTs nanocomposite modified screen-printed electrode for the direct determination of urea, *Sci. Rep.*, 2023, **13**(1), 1–16.
52 H. S. Magar, B. A. Hemdan, H. R. M. Rashdan and R. Y. A. Hassan, Rapid and Selective Detection of Foodborne Pathogens Using a Disposable Bio-sensing System Designed by Stepwise Antibody Immobilization on AuNPs@Cu-MOF Nanocomposite, *J. Anal. Test*, 2024, **8**, 478–492.
53 A. B. A. Hammad, A. M. E. Nahrawy and A. M. Mansour, Structural and Optical Properties of Sol–Gel-Spin Coating Nanostructured Cadmium Zinc Nickel Phosphate (CZNP) Film and the Current Transport Properties of CZNP/p-Si-Based Diode, *Silicon*, 2024, **16**, 2049–2063.
54 Md. Elias, S. Akter, Md. A. Hossain and M. H. Suhag, Fabrication of Zn3(PO4)2/carbon nanotubes nanocomposite thin film via sol-gel drop coating method with enhanced photocatalytic activity, *Thin Solid Films*, 2021, **717**, 138472.
55 R. D. Shannon, Revised effective ionic radii and systematic studies of interatomic distances in halides and chalcogenides, *Acta Crystallogr., Sect. A*, 1976, **32**, 751–767.
56 T. Ben Hamed, A. Boukhris, B. Glorieux and M. Ben Amara, Synthesis, crystal structure and spectroscopic characterization of a new cadmium phosphate, Na2Cd5(PO4)4, *J. Mol. Struct.*, 2020, **1199**, 126963.
57 M. Doumeng, L. Makhlouf, F. Berthet, O. Marsan, K. Delbé, J. Denape and F. Chabert, A comparative study of the crystallinity of polyetheretherketone by using density, DSC, XRD, and Raman spectroscopy techniques, *Polym. Test.*, 2021, **93**, 106878.
58 T. A. Hameed, A. R. Wassel and I. M. El Radaf, Investigating the effect of thickness on the structural, morphological, optical and electrical properties of AgBiSe2 thin films, *J. Alloys Compd.*, 2019, **805**, 1–11.
59 A. E. Rakhshani, Sn-rich CZTS films spin-coated from methanol-based sol-gel solution: annealing effect on microstructure and optoelectronic properties, *J. Sol-Gel Sci. Technol.*, 2020, **94**, 270–278.
60 A. B. Abou Hammad, A. M. Mansour and A. M. El Nahrawy, Ni2+doping effect on potassium barium titanate nanoparticles: enhancement optical and dielectric properties, *Phys. Scr.*, 2021, **96**, 125821.
61 A. M. El Nahrawy, B. A. Hemdan, A. M. Mansour, A. Elzwawy and A. B. Abou Hammad, Integrated use of nickel cobalt aluminoferrite/Ni2+ nano-crystallites supported with SiO2 for optomagnetic and biomedical applications, *Mater. Sci. Eng.: B*, 2021, **274**, 115491.
62 T. Dippong, E. A. Levei, O. Cadar, I. G. Deac, L. Diamandescu and L. Barbu-Tudoran, Effect of nickel content on structural, morphological and magnetic properties of NixCo1-xFe2O4/SiO2 nanocomposites, *J. Alloys Compd.*, 2019, **786**, 330–340.
63 A. B. Abou Hammad, B. A. Hemdan and A. M. El Nahrawy, Facile synthesis and potential application of Ni0.6Zn0.4Fe2O4 and Ni0.6Zn0.2Ce0.2Fe2O4 magnetic nanocubes as a new strategy in sewage treatment, *J. Environ. Manage.*, 2020, **270**, 110816.
64 V. Mote, Y. Purushotham and B. Dole, Williamson-Hall analysis in estimation of lattice strain in nanometer-sized ZnO particles, *J. Theor. Appl. Phys.*, 2012, **6**, 6.
65 K. Venkateswarlu, A. Chandra Bose and N. Rameshbabu, X-ray peak broadening studies of nanocrystalline hydroxyapatite by Williamson–Hall analysis, *Phys. B*, 2010, **405**, 4256–4261.

66 A. M. Mansour, B. A. Hemdan, A. Elzwawy, A. B. Abou Hammad and A. M. El Nahrawy, Ecofriendly synthesis and characterization of Ni2+ codoped silica magnesium zirconium copper nanoceramics for wastewater treatment applications, *Sci. Rep.*, 2022, **12**, 9855.
67 T. A. Taha, A. A. Azab and M. A. Sebak, Glycerol-assisted sol-gel synthesis, optical, and magnetic properties of NiFe2O4 nanoparticles, *J. Mol. Struct.*, 2019, **1181**, 14–18.
68 R. R. Prabhu and M. A. Khadar, Study of optical phonon modes of CdS nanoparticles using Raman spectroscopy, *Bull. Mater. Sci.*, 2008, **31**, 511–515.
69 B. Bharti, P. B. Barman and R. Kumar, XRD analysis of undoped and Fe doped TiO2 nanoparticles by Williamson Hall method, in *AIP Conference Proceedings*, AIP Publishing, 2015, vol. 1675, p. 030025.
70 M. Morsy, A. I. Abdel-Salam, D. A. Rayan, I. Gomaa and A. Elzwawy, Oil/water separation and functionality of smart carbon nanotube–titania nanotube composite, *J. Nanopart. Res.*, 2022, **24**, 226.
71 S. K. Pandey, S. K. Pandey, C. Mukherjee, P. Mishra, M. Gupta, S. R. Barman, S. W. D'Souza and S. Mukherjee, Effect of growth temperature on structural, electrical and optical properties of dual ion beam sputtered ZnO thin films, *J. Mater. Sci.: Mater. Electron.*, 2013, **24**, 2541–2547.
72 N. Kamarulzaman, M. F. Kasim and N. F. Chayed, Elucidation of the highest valence band and lowest conduction band shifts using XPS for ZnO and Zn0.99Cu0.01O band gap changes, *Results Phys.*, 2016, **6**, 217–230.
73 S. Chandrasekaran, L. Yao, L. Deng, C. Bowen, Y. Zhang, S. Chen, Z. Lin, F. Peng and P. Zhang, Recent advances in metal sulfides: From controlled fabrication to electrocatalytic, photocatalytic and photoelectrochemical water splitting and beyond, *Chem. Soc. Rev.*, 2019, **48**, 4178–4280.
74 R. M. Navarro, F. del Valle and J. L. G. Fierro, Photocatalytic hydrogen evolution from CdS–ZnO–CdO systems under visible light irradiation: Effect of thermal treatment and presence of Pt and Ru cocatalysts, *Int. J. Hydrogen Energy*, 2008, **33**, 4265–4273.
75 M. Gao, J. Yao, Y. Quan, J. Yang, P. Huo, J. Dai, Y. Yan and C. Ma, Neodymium doped zinc oxide for ultersensitive SERS substrate, *J. Mater. Sci.: Mater. Electron.*, 2019, **30**, 20537–20543.
76 C. Venkata Reddy, N. Bandaru, J. Shim and S. V. P. Vattikuti, Synthesis of CdO/ZnS heterojunction for photodegradation of organic dye molecules, *Appl. Phys. A: Mater. Sci. Process.*, 2017, **123**, 1–12.
77 A. Sahai and N. Goswami, Structural and optical investigations of oxygen defects in zinc oxide nanoparticles, *AIP Conf. Proc.*, 2015, 1665.
78 M. Gao, J. Yao, Y. Quan, J. Yang, P. Huo, J. Dai, Y. Yan and C. Ma, Neodymium doped zinc oxide for ultersensitive SERS substrate, *J. Mater. Sci.: Mater. Electron.*, 2019, **30**, 20537–20543.
79 W. S. AbuShanab, E. B. Moustafa and A. H. Hammad, Dependence of the structure, optical, and dynamic properties of novel cadmium phosphate glass on vanadium content, *J. Mater. Res. Technol.*, 2020, **9**, 14178–14189.
80 X. Z. Zhai, J. Qu, S. M. Hao, Y. Q. Jing, W. Chang, J. Wang, W. Li, Y. Abdelkrim, H. Yuan and Z. Z. Yu, Layered Birnessite Cathode with a Displacement/Intercalation Mechanism for High-Performance Aqueous Zinc-Ion Batteries, *Nanomicro Lett.*, 2020, **12**, 1–15.
81 Y. Wang and P. M. A. Sherwood, Phosphorus Pentoxide (P2O5) by XPS, *Surf. Sci. Spectra*, 2002, **9**, 159–165.
82 H. Wang, H. Guo, N. Zhang, Z. Chen, B. Hu and X. Wang, Enhanced Photoreduction of U(VI) on C3N4 by Cr(VI) and Bisphenol A: ESR, XPS, and EXAFS Investigation, *Environ. Sci. Technol.*, 2019, **53**, 6454–6461.
83 J. Winiarski, W. Tylus, K. Winiarska, I. Szczygieł and B. Szczygieł, XPS and FT-IR Characterization of Selected Synthetic Corrosion Products of Zinc Expected in Neutral Environment Containing Chloride Ions, *J. Spectrosc.*, 2018, **2018**, 2079278.
84 K. S. W. Sing, D. H. Everett, R. A. W. Haul, L. Moscou, R. A. Pierotti, J. Rouquerol and T. Siemieniewska, Reporting Physisorption Data for Gas/Solid Systems with Special Reference to the Determination of Surface Area and Porosity, *Pure Appl. Chem.*, 1985, **57**, 603–619.
85 L. C. Lin, M. Thirumavalavan, Y. T. Wang and J. F. Lee, Surface area and pore size tailoring of mesoporous silica materials by different hydrothermal treatments and adsorption of heavy metal ions, *Colloids Surf., A*, 2010, **369**, 223–231.
86 S. J. Gregg, K. S. W. Sing and H. W. Salzberg, Adsorption Surface Area and Porosity, *J. Electrochem. Soc.*, 1967, **114**, 279Ca.
87 S. Brunauer, P. H. Emmett and E. Teller, Adsorption of Gases in Multimolecular Layers, *J. Am. Chem. Soc.*, 1938, **60**, 309–319.
88 A. M. Mansour, Thermal microscopy (TM), *Int. J. Microstruct. Mater. Prop.*, 2020, **15**, 215–228.
89 D. D. Souza, J. Nettar and K. P. Nagaraja, Thermal, optical and electrical properties of cadmium doped zinc phosphate crystals, *AIP Conf. Proc.*, 2020, **2244**, 030001.
90 A. B. Abou Hammad, A. M. Mansour and A. M. El Nahrawy, Ni^{2+} doping effect on potassium barium titanate nanoparticles: enhancement optical and dielectric properties, *Phys. Scr.*, 2021, **96**, 125821.
91 A. B. A. Hammad, A. M. E. Nahrawy and A. M. Mansour, Structural and Optical Properties of Sol–Gel-Spin Coating Nanostructured Cadmium Zinc Nickel Phosphate (CZNP) Film and the Current Transport Properties of CZNP/p-Si-Based Diode, *Silicon*, 2024, **16**, 2049–2063.
92 A. R. Lowe, M. A. Chorażewski, Y. Grosu and Y. G. Bushuev, Energetic Characteristics of Hydrophobic Porous Materials as Candidates for Manufacturing of Nanorockets, *J. Phys. Chem. Lett.*, 2024, 12112–12119.
93 H. J. De Jager and L. C. Prinsloo, The dehydration of phosphates monitored by DSC/TGA and in situ Raman spectroscopy, *Thermochim. Acta*, 2001, **376**, 187–196.

94 A. G. C. Sales, B. R. S. Ibiapina, G. S. Sales, J. F. Cruz-Filho, A. E. B. Lima, G. L. da Paz, R. R. P. Garcia, A. Correa, B. C. Viana, G. O. M. Gusmão, C. C. Santos and G. E. Luz, Heat treatment influence on structural and optical properties of NiWO4 crystals, *J. Solid State Chem.*, 2023, **318**, 123773.

95 P. E. González Vargas, J. E. Morales-Mendoza, J. L. Domínguez-Arvizu, B. C. Hernández-Majalca, J. L. Bueno-Escobedo, A. B. Jasso Salcedo, L. I. Ibarra-Rodríguez, V. H. Collins-Martínez and A. López-Ortiz, NiWO4 self supported oxygen carrier for the chemical looping steam methane reforming, *Int. J. Hydrogen Energy*, 2025, DOI: 10.1016/j.ijhydene.2025.01.477.

96 A. M. El Nahrawy, A. M. Mansour, A. B. Abou Hammad, R. S. Ibrahim, A. M. Abouelnaga and M. S. Abdel-Aziz, Optical, Functional Impact and Antimicrobial of Chitosan/Phosphosilicate/Al2O3 Nanosheets, *J. Inorg. Organomet. Polym. Mater.*, 2020, **30**, 3084–3094.

97 A. M. El Nahrawy, A. Elzwawy, A. B. Abou Hammad and A. M. Mansour, Influence of NiO on structural, optical, and magnetic properties of Al2O3–P2O5–Na2O magnetic porous nanocomposites nucleated by SiO2, *Solid State Sci.*, 2020, **108**, 106454.

98 A. B. Djuriić, A. M. C. Ng and X. Y. Chen, ZnO nanostructures for optoelectronics: material properties and device applications, *Prog. Quantum Electron.*, 2010, **34**, 191–259.

99 V. Siva, K. Park, M. S. Kim, Y. J. Kim, G. J. Lee, M. J. Kim and Y. M. Song, Mapping the structural, electrical, and optical properties of hydrothermally grown phosphorus-doped zno nanorods for optoelectronic device applications, *Nanoscale Res. Lett.*, 2019, **14**, 1–9.

100 J. S. Stroud, Optical Absorption and Color Caused by Selected Cations in High-Density, Lead Silicate Glass, *J. Am. Ceram. Soc.*, 1971, **54**, 401–406.

101 B. B. Das, A. Srinivassan and M. Yogapriya, Structure-Property Relations in xWO3-0.31P2O5-0.31B2O3-(0.38-x) Cs2O (0.01 ≤ x ≤0.28) Glasses by IR, UV and EPR Spectroscopic Studies, *Chem. Chem. Eng.*, 2011, **5**, 369–375.

102 N. Venkatachalam, M. Palanichamy, B. Arabindoo and V. Murugesan, Retracted: Enhanced photocatalytic degradation of 4-chlorophenol by Zr4+ doped nano TiO2, *J. Mol. Catal. A:Chem.*, 2007, **266**, 158–165.

103 A. M. ElNahrawy, A. M. Mansour, H. A. ElAttar, E. M. M. Sakr, A. A. Soliman and A. B. A. Hammad, Impact of Mn-substitution on structural, optical, and magnetic properties evolution of sodium–cobalt ferrite for opto-magnetic applications, *J. Mater. Sci.: Mater. Electron.*, 2020, **31**, 6224–6232.

104 A. M. El Nahrawy, A. B. Abou Hammad and A. M. Mansour, Compositional Effects and Optical Properties of P2O5 Doped Magnesium Silicate Mesoporous Thin Films, *Arabian J. Sci. Eng.*, 2021, **46**, 5893–5906.

105 A. M. Mansour, A. B. A. Hammad and A. M. E. Nahrawy, Study on Optical of Chitosan-Aminopropyltriethoxysilane-SiO2 Nanocomposite Decorated with Carbon Nanotubes, *Silicon*, 2024, **16**, 147–155.

106 S. E. Ibrahim, I. A. El-Mesady, M. M. Semary and S. M. Othman, Physical, thermal and optical properties of Cd-doped phosphate based glass system, *Radiat. Phys. Chem.*, 2023, **209**, 110955.

107 R. S. Ibrahim, A. A. Azab and A. M. Mansour, Synthesis and structural, optical, and magnetic properties of Mn-doped CdS quantum dots prepared by chemical precipitation method, *J. Mater. Sci.: Mater. Electron.*, 2021, **32**, 19980–19990.

108 C. A. Hogarth and M. A. Ghauri, The preparation of cadmium phosphate and cadmium zinc phosphate glasses and their electrical and optical properties, *J. Mater. Sci.*, 1979, **14**, 1641–1646.

109 J.-Y. Chung, J.-H. Kim, S.-Y. Choi, H.-J. Park, M.-K. Hwang, Y.-K. Jeong, B.-K. Ryu, J.-Y. Chung, J.-H. Kim, S.-Y. Choi, H.-J. Park, M.-K. Hwang, Y.-K. Jeong and B.-K. Ryu, Structural, Optical, and Chemical Properties of Cadmium Phosphate Glasses, *J. Korean Ceram. Soc.*, 2015, **52**, 128.

110 A. B. Abou Hammad, A. A. Al-esnawy, A. M. Mansour and A. M. El Nahrawy, Synthesis and characterization of chitosan-corn starch-SiO2/silver eco-nanocomposites: Exploring optoelectronic and antibacterial potential, *Int. J. Biol. Macromol.*, 2023, **249**, 126077.

111 H. M. Gomaa, I. S. Yahia and H. Y. Zahran, Correlation between the static refractive index and the optical bandgap: Review and new empirical approach, *Phys. B*, 2021, **620**, 413246.

112 J. A. Duffy, Ultraviolet transparency of glass: A chemical approach in terms of band theory, polarisability and electronegativity, *Phys. Chem. Glasses*, 2001, **42**, 151–157.

113 R. R. Reddy, K. Rama Gopal, Y. Nazeer Ahammed, K. Narasimhulu, L. Siva Sankar Reddy and C. V. Krishna Reddy, Correlation between optical electronegativity, molar refraction, ionicity and density of binary oxides, silicates and minerals, *Solid State Ionics*, 2005, **176**, 401–407.

114 L. Pauling, The nature of the chemical bond. IV. The energy of single bonds and the relative electronegativity of atoms, *J. Am. Chem. Soc.*, 1932, **54**, 3570–3582.

115 F. Hcini, S. Hcini, M. A. Wederni, B. Alzahrani, H. Al Robei, K. Khirouni, S. Zemni and M. L. Bouazizi, Structural, optical, and dielectric properties for Mg0·6Cu0·2Ni0·2Cr2O4 chromite spinel, *Phys. B*, 2022, **624**, 413439.

116 A. Chandran and K. C. George, Defect induced modifications in the optical, dielectric, and transport properties of hydrothermally prepared ZnS nanoparticles and nanorods, *J. Nanopart. Res.*, 2014, **16**, 1–17.

117 Poonam, K. Sharma, A. Arora and S. K. Tripathi, Review of supercapacitors: Materials and devices, *J. Energy Storage*, 2019, **21**, 801–825.

118 C. An, Y. Zhang, H. Guo and Y. Wang, Metal oxide-based supercapacitors: progress and prospectives, *Nanoscale Adv.*, 2019, **1**, 4644–4658.

119 T. F. Yi, H. Chang, T. T. Wei, S. Y. Qi, Y. Li and Y. R. Zhu, Approaching high-performance electrode materials of

ZnCo2S4 nanoparticle wrapped carbon nanotubes for supercapacitors, *J. Mater.*, 2021, **7**, 563–576.

120 M. Guo, S. Wang, L. Zhao and Z. Guo, High-performance asymmetric supercapacitor based on flowery nickel-zinc phosphate microspheres with carbon dots, *Electrochim. Acta*, 2018, **292**, 299–308.

121 C. Zhao, S. Wang, Z. Zhu, P. Ju, C. Zhao and X. Qian, Roe-shaped Ni3(PO4)2/RGO/Co3(PO4)2 (NRC) nanocomposite grown in situ on Co foam for superior supercapacitors, *J. Mater. Chem. A*, 2017, **5**, 18594–18602.

122 M. Yi, F. Xiang, X. Yue, X. Zhou, N. Jiang, Q. Zheng and D. Lin, Porous Ni2P/Co2(P2O7) heterojunction nanosheets as an advanced electrode for high-performance supercapacitors, *Appl. Surf. Sci.*, 2022, **604**, 154503.

123 F. S. Omar, A. Numan, S. Bashir, N. Duraisamy, R. Vikneswaran, Y. L. Loo, K. Ramesh and S. Ramesh, Enhancing rate capability of amorphous nickel phosphate supercapattery electrode via composition with crystalline silver phosphate, *Electrochim. Acta*, 2018, **273**, 216–228.

124 H. Pang, Z. Yan, Y. Ma, G. Li, J. Chen, J. Zhang, W. Du and S. Li, Cobalt pyrophosphate nano/microstructures as promising electrode materials of supercapacitor, *J. Solid State Electrochem.*, 2013, **17**, 1383–1391.

125 M. S. Javed, A. J. Khan, A. Ahmad, S. H. Siyal, S. Akram, G. Zhao, A. A. Awadh Bahajjaj, M. Ouladsmane and M. Alfakeer, Design and fabrication of bimetallic oxide nanonest-like structure/carbon cloth composite electrode for supercapacitors, *Ceram. Int.*, 2021, **47**, 30747–30755.

126 S. Fleischmann, J. B. Mitchell, R. Wang, C. Zhan, D. E. Jiang, V. Presser and V. Augustyn, Pseudocapacitance: From Fundamental Understanding to High Power Energy Storage Materials, *Chem. Rev.*, 2020, **120**, 6738–6782.

127 C. Choi, D. S. Ashby, D. M. Butts, R. H. DeBlock, Q. Wei, J. Lau and B. Dunn, Achieving high energy density and high power density with pseudocapacitive materials, *Nat. Rev. Mater.*, 2019, **5**(1), 5–19.

128 H. S. Magar, R. Y. A. Hassan and M. N. Abbas, Non-enzymatic disposable electrochemical sensors based on CuO/Co3O4@MWCNTs nanocomposite modified screen-printed electrode for the direct determination of urea, *Sci. Rep.*, 2023, **13**(1), 1–16.

129 N. H. Mahmoud, H. S. Magar, M. G. Rizk and A. M. Fahim, Comparative, synthesis, ADME studies, and electrochemical studies, of the divalent and monovalent binuclear complexes of malonate derivatives, *J. Mol. Struct.*, 2024, **1305**, 137717.

130 J. He, X. Xu, M. Li, S. Zhou and W. Zhou, Recent advances in perovskite oxides for non-enzymatic electrochemical sensors: A review, *Anal. Chim. Acta*, 2023, 1251.